AD_____

Award Number: DAMD17-98-1-8231

TITLE: A Computational Approach Toward Identification of Malignant Lesions of the Human Breast: The Dynamics of Magnetic Resonance Imaging Contrast Agent Uptake

PRINCIPAL INVESTIGATOR: Jonathan H. Kaufman, Ph.D.
John S. Leigh, Ph.D.

CONTRACTING ORGANIZATION: University of Pennsylvania
Philadelphia, Pennsylvania 19104-3246

REPORT DATE: September 1999

TYPE OF REPORT: Annual Summary

PREPARED FOR: U.S. Army Medical Research and Materiel Command
Fort Detrick, Maryland 21702-5012

REPORT DOCUMENTATION PAGE

Form Approved
OMB No. 074-0188

1. AGENCY USE ONLY (Leave blank)	2. REPORT DATE	3. REPORT TYPE AND DATES COVERED
	September 1999	Annual Summary (1 Sep 98 - 31 Aug 99)

4. TITLE AND SUBTITLE
A Computational Approach Toward Identification of Malignant Lesions of the Human Breast: The Dynamics of Magnetic Resonance Imaging Contrast Agent Uptake

5. FUNDING NUMBERS
DAMD17-98-1-8231

6. AUTHOR(S)
Jonathan H. Kaufman, Ph.D.
John S. Leigh, Ph.D.

7. PERFORMING ORGANIZATION NAME(S) AND ADDRESS(ES)
University of Pennsylvania
Philadelphia, Pennsylvania 19104-3246

E-MAIL:
jonathak@mail.med.upenn.edu

8. PERFORMING ORGANIZATION REPORT NUMBER

9. SPONSORING / MONITORING AGENCY NAME(S) AND ADDRESS(ES)
U.S. Army Medical Research and Materiel Command
Fort Detrick, Maryland 21702-5012

10. SPONSORING / MONITORING AGENCY REPORT NUMBER

11. SUPPLEMENTARY NOTES

12a. DISTRIBUTION / AVAILABILITY STATEMENT
Approved for public release; distribution unlimited

12b. DISTRIBUTION CODE

13. ABSTRACT ***(Maximum 200 Words)***

Dynamic Gd-DTPA-2 contrast enhanced MRI images are currently used to help identify the malignancy of breast lesions. The time course of contrast agent uptake may thus be a non-invasive method for discriminating benign vs. malignant breast lesions. In this study, a computational technique called fuzzy clustering is employed to empirically categorize voxels of breast MRI images based on the time course of contrast agent enhanced image intensity. Several parameters of the clustering algorithm have been optimized including the fuzzy index and cluster membership thresholds. The clustering algorithm has been able to discriminate contrast uptake heterogeneity within breast lesions, and central vs. peripheral regions. These two features have not, on their own, discriminated malignant vs. benign lesions.

14. SUBJECT TERMS
Breast Cancer

15. NUMBER OF PAGES
34

16. PRICE CODE

17. SECURITY CLASSIFICATION OF REPORT	18. SECURITY CLASSIFICATION OF THIS PAGE	19. SECURITY CLASSIFICATION OF ABSTRACT	20. LIMITATION OF ABSTRACT
Unclassified	Unclassified	Unclassified	Unlimited

FOREWORD

Opinions, interpretations, conclusions and recommendations are those of the author and are not necessarily endorsed by the U.S. Army.

___ Where copyrighted material is quoted, permission has been obtained to use such material.

___ Where material from documents designated for limited distribution is quoted, permission has been obtained to use the material.

___ Citations of commercial organizations and trade names in this report do not constitute an official Department of Army endorsement or approval of the products or services of these organizations.

N/A In conducting research using animals, the investigator(s) adhered to the "Guide for the Care and Use of Laboratory Animals," prepared by the Committee on Care and use of Laboratory Animals of the Institute of Laboratory Resources, national Research Council (NIH Publication No. 86-23, Revised 1985).

N/A For the protection of human subjects, the investigator(s) adhered to policies of applicable Federal Law 45 CFR 46.

N/A In conducting research utilizing recombinant DNA technology, the investigator(s) adhered to current guidelines promulgated by the National Institutes of Health.

N/A In the conduct of research utilizing recombinant DNA, the investigator(s) adhered to the NIH Guidelines for Research Involving Recombinant DNA Molecules.

N/A In the conduct of research involving hazardous organisms, the investigator(s) adhered to the CDC-NIH Guide for Biosafety in Microbiological and Biomedical Laboratories.

12/30/99

PI - Signature Date

TABLE OF CONTENTS

INTRODUCTION

Subject: This project optimizes and evaluates a computational clustering technique for aiding the diagnostician to discriminate malignant breast lesions during a post contrast agent injection time series of three-dimensional MRI images. *Purpose:* Currently, few diagnosticians are skilled in the art of identifying malignancy from these images. It is possible that the contrast agent may diffuse into and out of malignant tumors with a unique time course signature discernable via a fuzzy clustering algorithm. *Scope:* The project employs an existing fuzzy clustering algorithm previously used to discriminate brain tissues. Several computational parameters must be optimized for he clustering algorithm to be useful in the setting of breast lesions, and the usefulness of the technique in discriminating malignant vs. benign lesions must ultimately be evaluated.

BODY

Background and Introduction

The Fuzzy Clustering Algorithm Implimentation

The fuzzy clustering analysis (FCA) properties of robustness and being unbiased are exactly the characteristics which make FCA an attractive method for analysis of dynamic gadolinium time course curves.

An advantage of using fuzzy clustering is its ability to separate the gadolinium uptake data into K distinct clusters. As we have implemented it, associated with each of the K clusters is a temporal cluster centroid and a cluster membership map. The temporal centroid displays the temporal course of the gadolinium enhancement. It is calculated as the weighted mean of the normalized temporal data, where the weight of each temporal course is proportional to the corresponding membership to the cluster. Thus temporal courses that have high membership to a cluster contribute strongly to the cluster centroid, whereas temporal courses with low membership do not.

The cluster membership map gives the "degree of belonging" of each voxel to the cluster; it displays where in the breast the gadolinium uptake curve depicted by the corresponding cluster centroid occurred. As opposed to hard clustering algorithms, for which the weights are either one or zero (i.e., belonging, or not belonging), the fuzzy clustering algorithm associates a fuzzy membership (a value between zero and one) for each spatial location (i.e., each voxel) to each of the K clusters. The fuzzy membership is analogous, but not equivalent, to the probability of belonging to the cluster. This more realistically represents the dynamic processes that occur in perfusion breast data.

Statement of Work (First 18 Months)

Task 1. To segment breast tissue on the basis of MR image contrast enhancement kinetics. Determine the fuzzy index and threshold for membership in a cluster. *(months 1 to 8).* **(Status: complete. See methods and materials computation seciton.)** Determine the "normalization or preparation of the time course data needed for presenting the images to the fuzzy clustering algorithm. *(months 1 to 12).* **(Status: in progress)** Using the parameters determined above, perform fuzzy clustering on 300 image data sets and determine the sensitivity of the fuzzy clustering for detecting breast abnormalities. *(months 12 to 24).* **(Status: completed 43 of the 300 sets.)**

Methods and Materials

Patient Population

To date we have performed fuzzy clustering analysis on 43 breast MRI cases. Breast images from seven women are used here. All subjects were selected for MRI because they had a suspicious finding on mammography or a palpable lesion and were also scheduled for excisional biopsy.

MR Image Acquisition

Magnetic resonance images (1.5T) of the breast were obtained using 3D volume fast rf-spoiled gradient echo imaging scheme with fat suppression. To obtain 3D images in 90 seconds, a partial data acquisition scheme with 32 kHz acquisition bandwidth was used which allowed TR times of 9.9 msec. The TE time was 2.2 msec and provides fat/water opposed-phase images. The flip angle of the excitation pulse was 45 degrees. The fat suppression pulse consists of a frequency selective inversion pulse applied at the largest lipid resonance (220 Hz from water) once every 16 TRs. The inversion delay for

best fat suppression was optimized empirically. The image acquisition consists of a data matrix of 512 x 256 x 32 resulting in an image with 512 x 512 x 28 matrix. The field of view of the images is 18 cm with a slice thickness that ranged from 0.7 to 3 mm depending on the size of the breast. The slices are in the sagittal plane. To attain sufficient signal-to-noise for these high spatial resolution images, a four coil receive array was used. The breast was lightly compressed between two plates which contain two coils each. The compression helped the breast to fill the 18 cm square FOV while narrowing the breast in the slice direction. For all studies, one pre- and four post-gadolinium images were obtained at 90 second time resolution.

Computations

Regions of significant gadolinium uptake can be defined from the cluster membership map of each cluster by thresholding the map at a selected level of membership. This thresholding process creates partitions (i.e., groups) from the clusters. A threshold of 0.80 to 0.90 typically performed well. Higher values would be ineffective because the presence of noise.

Intrinsic to the fuzzy clustering algorithm is the fuzzy index, m ($m > 1.0$), which controls the "fuzziness" of the clusters. A value near one results in "hard" clusters, whereas larger values result in successively more "fuzzy" clusters. A compromise between hard and fuzzy clusters was found to be $m = 1.2$, which has been used successfully. This value has also been supported by studies of both simulated and actual fMRI data.

Results and Discussion

Data Summary

Space limitation preclude the possibility of conveying images for the 43 cases acuired to date. Typical results are shown for cases representing a benign lesion, ductal carcinoma, fibroadenoma, and lobular carcinoma.

Benign Lesion

Figure 1 shows the results of a first pass FCA in a breast with a benign lesion. The two clusters containing uptake curves with significant enhancement gives the parenchyma and the lesion (clusters 1 and 2). Clustering on shape of the curve redistributes the pixels in clusters 1 and 2 from the first pass into four clusters (Fig. 2). The pixels within the lesion are primarily in cluster 1. The centroid for cluster 1 shows a peak in enhancement at 90 milliseconds.

Figure 1

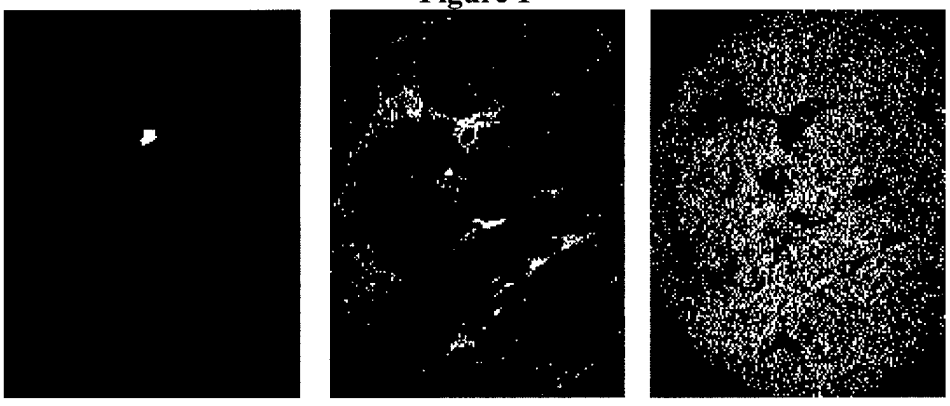

Figure 2

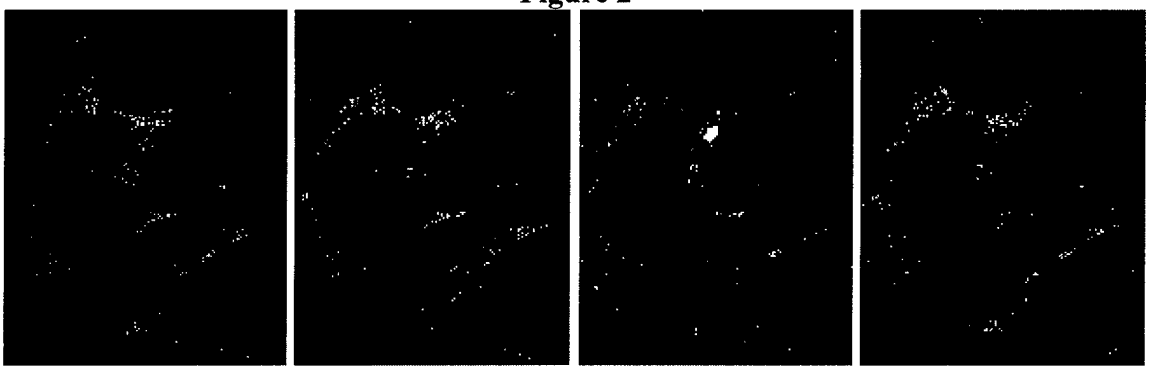

Ductal Carcinoma

Figure 3 shows the centroids and membership map of cluster corresponding to centroid 4 for three slices of this breast. There are two lesions, one in the first slice and another in the third. Partial voluming of both lesions in slice 2 can be observed as well as some pixels that bridge the region between them. The histopathology indicated two foci of invasive carcinoma with ductal carcinoma connecting the two lesions. The two lesions are easily picked up by the FCA as well as the bridging DCIS (ductal carcinoma in situ) in the intermediate slice. A third pass through the FCA on the lesion cluster gave three distinct clusters (see Fig 4). One cluster, 2, consists of the lesion while cluster 1 is predominantly found along the rim of the lesion. Careful examination of the borders of the lesion under the microscope revealed that it was bordered by areas DCIS.

Figure 3

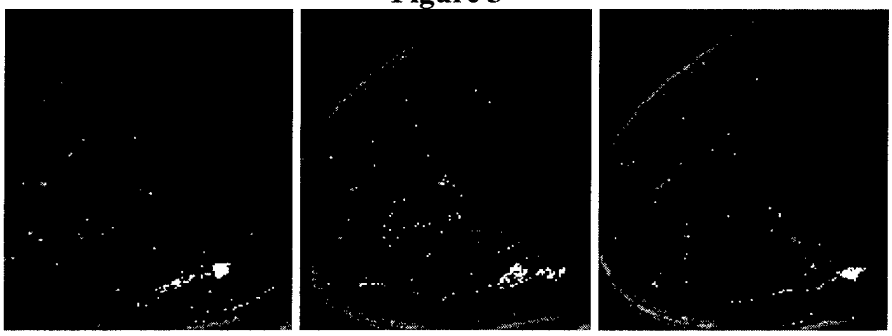

Figure 4

Fibroadenoma

In Figure 5, the one pre- and four post-contrast images of a fibroadenoma are shown as well as the centroids and pixels associated with each cluster. Unlike the invasive carcinoma in Fig. 3 and 4, the shape of the enhancement curve varies greatly across the lesion. This variation is not apparent in the post-contrast images themselves. However, like the invasive carcinoma, there is one cluster, 3, which is predominantly the rim of the lesion. On close examination of the histology slides, this fibroadenoma was found to be bordered nearly completely by blood vessels. The high spatial variation of the enhancement curves within the lesion may also be a result of the blood vessels inside the lesion.

Figure 5

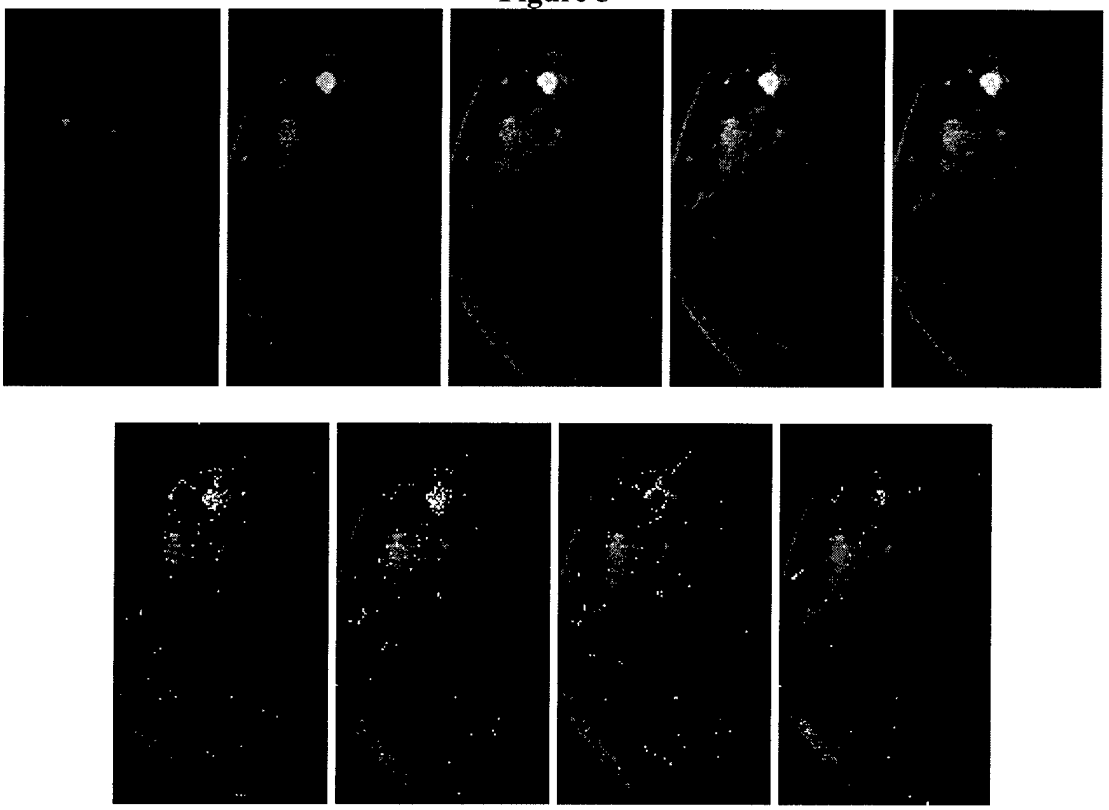

Lobular Carcinoma

Figure 6 shows the centroids and membership map of cluster four in 12 slices of a breast with extensive lobular carcinoma in situ (LCIS). In the post-contrast images, this breast would be specified as having regional enhancement. The images how that there are two dominate regions of enhancement, one in the more medial slices in the upper region of the breast and the second in the lateral slices in the middle of the breast. There are also blood vessels in the lateral slices at the top of the breast which proceed down the surface of the breast turning into the breast halfway down. This is more easily seen in a movie of 3D projections. In cases of regional enhancement, it is important to establish connectivity of the patches of enhancement in order to determine if it arises from one area and spreads of if there are two separate patches that developed independently.

Identifying blood vessels is also important. Biopsies were obtained from the two patches of enhancement and the pathologist identified the existence of LCIS in both areas. Unfortunately, histology cannot determine whether these two regions arise from the same source or are two independent sources. Based on the 3D FCA results, it appears as if these regions are connected spatially.

Figure 6

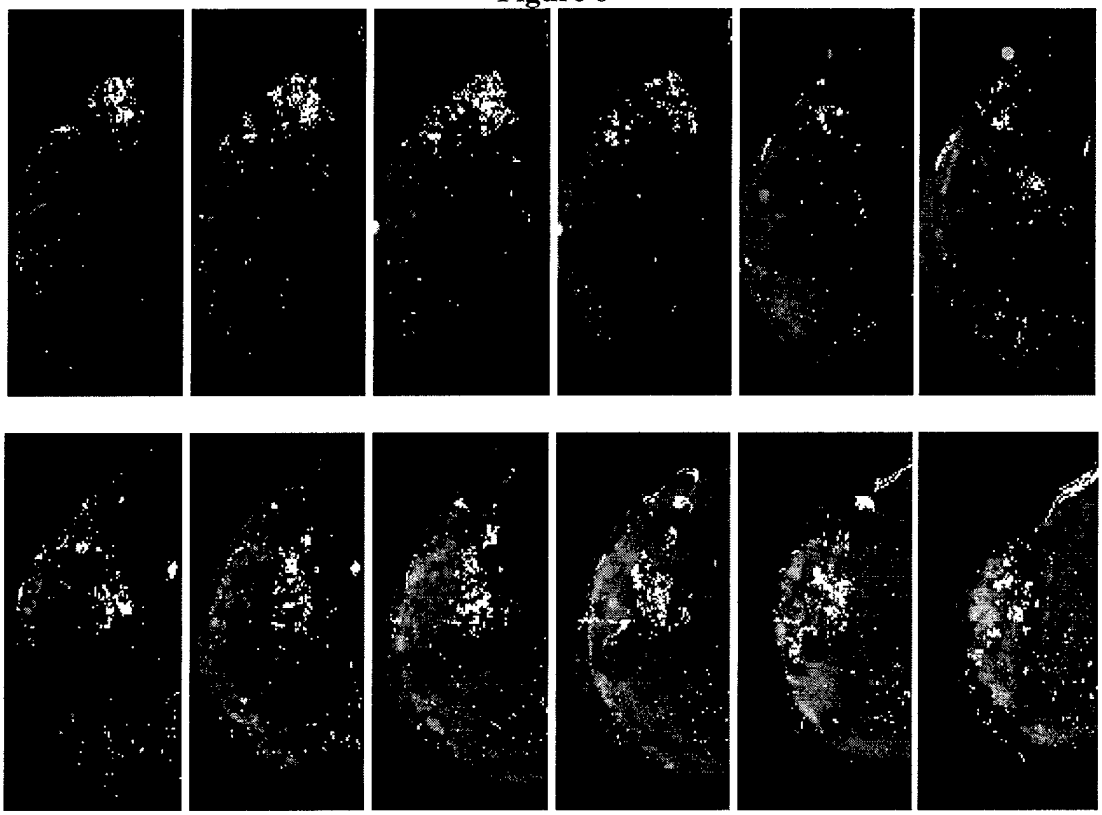

Conclusions

FCA was capable of determining the location of lesions or areas of LCIS/DCIS. However, by itself it cannot diagnose breast cancer. Other parameters such as architectural features and analysis of the time course curves can further aid in distinguishing benign from malignant disease. However, segmentation using FCA can point out areas of concern to the clinician which would aid in the diagnostic process. By performing this analysis on a large number of cases, uptake curves characteristic of various lesion types can be identified. Definition of these curves is independent of a model for contrast uptake. In the future, the characteristic curves could be used for both diagnosis and staging of breast cancer even when the lesions are small.

KEY RESEARCH ACCOMPLISHMENTS

- Determined optimal fuzzy index and membership threshold.
- Completed 43 Breast MRI studies which includes: benign lesions, ductal carcinomas, fibroadenomas, and lobular carcinomas.

REPORTABLE OUTCOMES

Since this is the first year of the project, publication of the results detailed in this progress have yet to be published; two manuscripts are in progress. During this first year period, the graduate student (PI) of this research fellowship has published the results of his previous academic rotation. Since stipend support was received during the period of these publications, they are appended.

- Sodium and Proton MR Properties of Cartilage During Compression. Regatte RR. Kaufman JH. Noyszewski EA. Reddy R. Journal of Magnetic Resonance Imaging. 10:961-967, 1999.
- A novel approach to observing articular cartilage deformation in-vitro via magnetic resonance imaging. Kaufman JH. Regatte RR. Bolinger L. Kneeland JB. Reddy R. Leigh JS. *Journal of Magnetic Resonance Imaging*. 9(5):653-662, 1999.
- Sodium NMR evaluation of articular cartilage degradation. Insko EK. Kaufman JH. Leigh JS. Reddy R. *Magnetic Resonance in Medicine*. 41(1):30-34, 1999.

JOURNAL OF MAGNETIC RESONANCE IMAGING 9:653–662 (1999)

Original Research

A Novel Approach to Observing Articular Cartilage Deformation In Vitro via Magnetic Resonance Imaging

Jonathan H. Kaufman, MS,* Ravinder Reddy Regatte, PhD, Lizann Bolinger, PhD, J. Bruce Kneeland, MD, Ravinder Reddy, PhD, and John S. Leigh, PhD

The design of a pressure cell that compresses a cartilage specimen in one dimension within an imaging magnet is presented. One-dimensional projection images in a direction perpendicular to the articular surface of the cartilage specimen were used to generate a uniaxial confined deformation creep curve for normal and trypsin-degraded cartilage specimens during a continuous 0.690 MPa (100 psi) pressure application. The resulting curves are shown to fit a two time constant viscoelastic model well and also indicate that the elastic modulus of cartilage decreases and the deformation rate increases upon trypsin proteolysis. Furthermore, cartilage permeability is shown as a function of cartilage strain for both the normal and trypsin-degraded case. Several two-dimensional slice-selective images were collected both before and after 80 minutes of continuous compression. These images were used to evaluate the relative changes in the spin-lattice, T1, and spin-spin, T2, relaxation time constant maps for both normal and degraded cartilage specimens in response to compression. The results of this study demonstrate the utility of a novel, non-magnetic, cartilage compression device and also support the validity of a simple two-component rheological model of articular cartilage. J. Magn. Reson. Imaging 1999;9:653–662. © 1999 Wiley-Liss, Inc.

Index terms: osteoarthritis; cartilage; compression; permeability; viscoelastic; MRI

ARTICULAR CARTILAGE is found at the surface of contacting bones in the synovial joints of mammals. Its role is primarily to allow low friction joint mobility. A second function of articular cartilage is to absorb mechanical shock when synovial joints experience impact during activities such as jogging. Osteoarthritis is a condition in which articular cartilage degradation occurs, leading to further joint abnormalities and in many cases to pain and loss of function (1). A non-invasive modality for detecting the earliest stages of osteoarthritis has yet to be developed (2). Such a non-invasive technique would be clinically useful in assessing joint abnormalities and would also be useful in assessing the efficacy of novel therapeutics.

In its normal condition, articular cartilage is a remarkable tissue in the sense that it is extremely firm while being composed primarily of water (3). Approximately 80% of the mass of articular cartilage is water. The remainder of the cartilage mass is composed for the most part of the solid matrix of collagen type II molecules and large proteoglycan aggregates (4). The composition of cartilage is actively maintained by chondrocytes, although compared with most tissues, cartilage is relatively acellular. The firm nature of articular cartilage results from a high osmotic pressure. The abundant proteoglycan aggregates are highly sulfated, leading to a high negative fixed charge density within the cartilage matrix. This fixed charge density attracts a large number of cations (primarily Na^+) into the cartilage matrix. The resulting large number of ions within the cartilage matrix attracts water at a high pressure to satisfy the Donnan equilibrium (5). However, there is evidence that other factors may contribute to the compressive strength of cartilage (6). This high pressure of water within the cartilage matrix gives the cartilage its stiffness, while the integrity of cartilage is maintained by the high tensile strength of the collagen framework.

The earliest stages of osteoarthritis are often characterized by a reduction of proteoglycan content (7–9). This compositional change is thought to be associated with initial cartilage softening, which is consistent with the intuitive notion that a reduction in proteoglycan content would reduce the osmotic pressure within the cartilage. Subsequent to this initial stage, the cartilage softening, in combination with mechanical wear, leads to a disruption of the collagen framework, leading to erosion of the articular surface of the cartilage followed by fissure and cracking.

The normal function of articular cartilage involves compression. As articular cartilage is compressed, the fluid contained within the cartilage matrix is extruded into the joint space. The extruded fluid acts as a lubricant between the contact points of opposing bone interfaces (10). It is possible that cartilage that is too soft will compress to an unnatural extent and provide a

MMRRCC, Department of Radiology, University of Pennsylvania School of Medicine, 422 Curie Blvd., Philadelphia, PA 19104.

Contract grant sponsor: NIH; contract grant numbers: RR02305 and R01AR45242-01.

*Address reprint requests to: J.H.K., MMRRCC, Department of Radiology, University of Pennsylvania School of Medicine, 422 Curie Blvd., Philadelphia, PA 19104.

Received July 17, 1998; Accepted January 15, 1999.

mechanical advantage for natural shear forces to disrupt the collagen framework. Additionally, soft cartilage may not be able to recover its original shape quickly enough to continue providing fluid to a bone interface during repeated loading. The experiment described in this manuscript characterizes several magnetic resonance imaging properties of articular cartilage specimens while simultaneously acquiring information regarding deformation.

MATERIALS AND METHODS

Pressure Cell Design

The pressure cell, shown in Fig. 1, consists of a pneumatically activated ceramic piston confined in a cylindrical chamber. The cartilage was positioned in the pressure cell with its articular surface in contact with a porous glass filter (Corning 31001-10F). The porous glass filter led to a drain that allowed extruded cartilage fluid to leave the cell. The pressure cell design inhibits lateral cartilage strain and only permits fluid to leave the cartilage via the articular surface.

The cylinder and cap of the pressure cell were made of Delrin (Dupont). This polymer exhibits no proton NMR signal, is nonmetallic, and has an electrical resistivity on the order of 10^{14} Ω-cm and a dissipation factor of 0.0048 at 10^6 Hz. The piston was made of a machinable ceramic, Macor (Corning). This ceramic has an electrical resistivity on the order of 10^{16} Ω-cm and a loss tangent of 10^{-3} at 1 kHz and 10^{-4} at 8.5 GHz. The pore size of the glass filter was chosen such that it was impermeable to the solid matrix of the cartilage but freely permeable to the cartilage fluid. The compressed air that pneumatically activated the piston was prevented from traveling around the sides of the piston by a Teflon seal. Pressure was applied via a compressed air tank and was measured by a digital pressure gauge (Omega DPG-500) on the regulator. A solenoid radiofrequency (RF) coil was wrapped around the cylinder of the pressure cell. The pressure cell was placed inside an 11

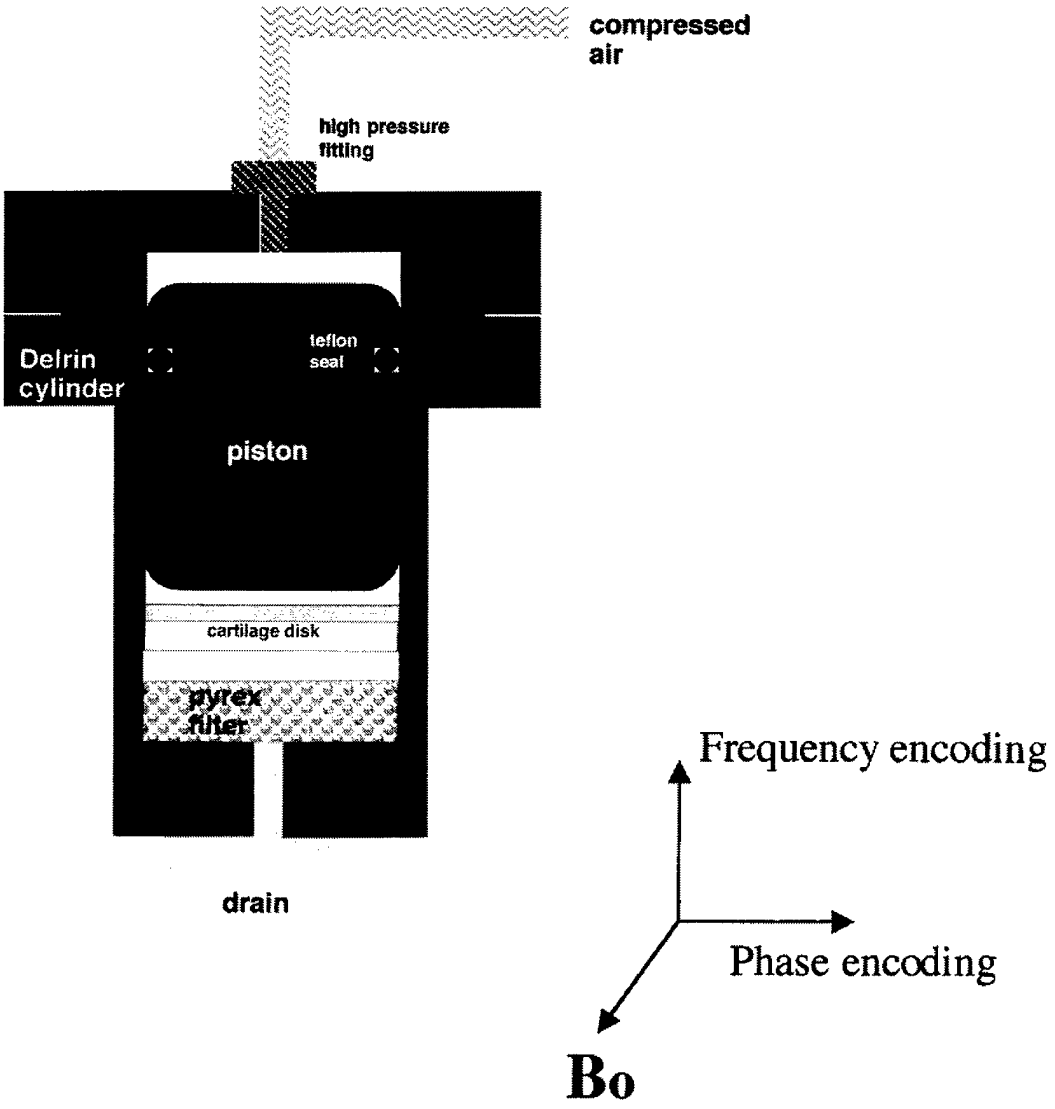

Figure 1. Cross-sectional diagram of MR-compatible pressure cell. Compressed air exerts a pressure on a piston that is confined in a cylindrical shaft. The piston, when responding to the pressure from the compressed air, pushes on the specimen that is positioned between the cylinder and a Pyrex filter, which allows cartilage fluid to extrude from the cell.

cm diameter local gradient set capable of generating 8 G/cm. The cell and gradient set were then placed in the 1 meter bore of a 2 T Oxford whole-body imaging magnet interfaced to a custom-built NMR spectrometer.

Uniaxial Confined Deformation Creep Experiment

The uniaxial confined deformation creep experiment was chosen as a method to measure the viscoelastic properties of the cartilage specimens. This experiment was first employed on cartilage specimens by Mow and coworkers (11). In this experiment, pressure is applied to the cartilage in the form of a step function. Prior to pressure application, a series of two-dimensional 90 °-180 ° spin-echo images was acquired. Upon compression, one-dimensional 90 °-180 °spin-echo image projections were acquired every 5 seconds for a period of 80 minutes. The compression was driven by a pressure of 0.690 MPa (100 psi), which was established within the first 20 seconds of the one-dimensional projection-image acquisition period and was maintained for the duration of the creep experiment. After the 80 minutes of constant pressure application, the pressure of 0.690 MPa was maintained for a subsequent set of two-dimensional image acquisitions.

Image Acquisition

Slice-selective images of each cartilage specimen in a plane coincident with a diameter of the cartilage disc and perpendicular to the cartilage surface were acquired. Slice thickness was 2 mm. In each case the cartilage specimen was oriented such that its articular surface was parallel to B_0, the main magnetic field. All two-dimensional images were acquired with a standard 90 °-180 °spin-echo RF pulse sequence. A 10 kHz bandwidth was used. The orientations of frequency and phase encoding are indicated in Fig. 1. Each image employed a 256 × 256 array of pixels. All images were acquired using a 2 T full-body imaging magnet integrated with a custom-built spectrometer. Local gradients sets that enclose the pressure cell were constructed that provide up to 8 gauss/cm. All RF pulses were applied via a solenoidal coil tuned to the proton frequency having six turns and a diameter of 2.5 cm. Imaging data were analyzed using the Interactive Display Language interpreter on a Silicon Graphics workstation.

Relaxation Time Mapping

We constructed maps of the spin-lattice, T1, and spin-spin, T2, relaxation times for each position of the cartilage imaging slice corresponding to an image pixel. In general, the relaxation time maps were constructed from fitting Eqs. [1] and [2]

$$I = A(1 - \exp(-\mathrm{TR}/\mathrm{T1})) + B \quad (1)$$

$$I = C \exp(-\mathrm{TE}/\mathrm{T2}) \quad (2)$$

where I is image intensity, TR is the repetition time, TE is the echo time, and A, B, C are arbitrary constants, to a series of 90 °-180 °spin-echo images employing different echo times and different repetition times. Five images were used to construct each T1 map. All were acquired with an echo time of 20 msec and had the following repetition times: 0.5, 1.0, 1.5, 2.0, and 2.5 seconds. Six images were used to construct each T2 map. All were acquired with a repetition time of 2.0 seconds and had the following echo times: 20, 30, 40, 50, 60, and 70 msec. The collected images were fit to Eqs. [1] and [2] using a gradient expansion algorithm for a non-linear least squares fit. It is important to note that this technique for mapping the T2 relaxation time constant is not independent of diffusion effects, and thus the T2 values that we report deviate from true T2 values since our method has not incorporated a diffusion-weighting factor (12,13). As early as 1954, Carr and Purcell (14) demonstrated that the contribution of diffusion when observing T2 decay with a series of individual spin echo events was

$$My_d = -M_0 \exp[\gamma^2 D t^3/12n^2], \quad (3)$$

where My_d is the contribution of diffusion, γ is the gyromagnetic ratio, D is the diffusion constant, t is duration that a spin ensemble experiences a gradient, and n is the number of echoes. Considering our experimental parameters of gradients no larger than 8 G/cm, and using a diffusion constant of 10^{-5} cm^2/sec, we estimate that diffusion can influence our T2 measurements by a factor of approximately 10%.

In addition, given the fixed set of repetition times, our method for mapping T1 has an inherent limitation on the range of T1 values. This limitation is especially important when considering T1 values near the lowest repetition time of 0.5 seconds. A calibration of our T1 mapping technique with copper sulfate-doped agarose phantoms of known T1 and cartilage specimens (where we measured bulk T1 with an inversion recovery technique) indicated that our T1 mapping procedure yielded T1 values accurate to within an approximate 50% range.

Cartilage Preparation

All cartilage specimens were obtained from the patella of bovine calves (ages ranged from 6 months to a year) within 10 hours from sacrifice. We obtained a total of 10 specimens, 5 of which were treated with trypsin as described in the next section. Cartilage specimens were harvested from the flat portion of the articular surface of the patella with a diamond core drill. With a small spatula, each disc was peeled from the cartilage-bone interface. Prior to insertion into the pressure cell, each specimen was equilibrated in 10 mL of phosphate-buffered saline (Sigma P-4417) at room temperature for 30 minutes.

Trypsin Degradation

In an effort to simulate articular cartilage in an early arthritic state, we exposed five cartilage specimens to a moderate proteolytic regime. Since it has been hypoth-

esized that early stages of osteoarthritis involve the loss of proteoglycan content selectively, we chose a proteolytic agent that would selectively deplete the proteoglycan content of the cartilage while leaving the collagen network relatively intact. The proteolytic enzyme trypsin is known to cleave the core proteins of the proteoglycans while having little effect on the type II collagen fibers that comprise the collagenous network of articular cartilage. The digested cartilage specimens referred to in this manuscript were generated by incubating each cartilage specimen in a 10 mL volume of 1 mg/mL trypsin (Sigma T-8253)/phosphate-buffered saline (Sigma P-4417) solution for 75 minutes at 37 ℃ with slight agitation.

RESULTS

Consistency of Results Among Samples

The five undigested specimens had, with respect to each other, a variation of maximal strains of 10% and a variation of deformation creep time constant of 40%. The results from the five trypsin-treated specimens had a similar degree of variation.

Viscoelastic Properties of Normal and Degraded Articular Cartilage

One method of measuring the mechanical properties of a viscoelastic material is with the uniaxial confined deformation creep experiment. In this method, a constant pressure is applied to the viscoelastic material as the deformation of the material is measured as a function of time (15). In the context of the experiment with cartilage, a first step is to keep the experimental parameters one-dimensional such that the analytical aspects are manageable (16). This is primarily possible with cartilage as a consequence of the tissue's natural deformation mechanism. Cartilage can be thought of as a substance that, in bulk, is incompressible unless fluid extrusion is permitted. We thus confined the cartilage discs laterally, while allowing fluid to extrude from the articular surface. In this way, both the pressure and the deformation are contained in one dimension, the direction perpendicular to the articular surface.

To measure the compressive response of the cartilage disc to the applied pressure, we derived the thickness of the cartilage specimen from the one-dimensional 90 °-180 ° spin-echo image projections that were acquired every 5 seconds over a period of 80 minutes. Six of these projections are shown in Fig. 2 as examples. The presence of signal intensity in these projections indicates the presence of protons, and for the most part also indicates the presence of the cartilage. Toward the left-hand side of the peak is a low-intensity plateau that corresponds to the water within the pores of the permeable glass filter. The representation of this projection does not have sharp edges. Two experimental factors contribute to this lack of sharpness. First, the cartilage specimen was not exactly perpendicular to the frequency-encoding direction. The tilt was slightly less than 3 °. Second, a susceptibility artifact existed at the interface between the cartilage specimen and the ceramic piston as well as between the cartilage specimen and the glass filter.

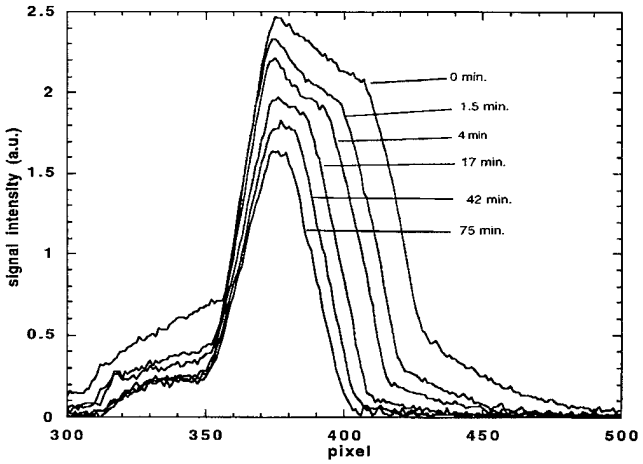

Figure 2. One-dimensional 90 °-180 °spin-echo projection images of the cartilage specimen. Six projections are shown at various times after onset of pressure application, as indicated. The plateau on the left corresponds to water held within the glass filter shown in Fig. 1. The left-hand slope of the projection corresponds to the articular surface of the cartilage specimen. The right-hand side of the projection corresponds to the cartilage-bone boundary. The compressive force is from right to left against the stationary glass filter.

The thickness of the cartilage was estimated as the full width of the projection at half its maximal value. The thickness calculation entailed a linear interpolation of signal intensity for regions between those represented by pixels. The thickness calculation was performed independently for each one-dimensional projection. The one-dimensional projection images were not collected beyond the 80-minute data acquisition period; it is likely, based on the trend of the creep curves, that the cartilage specimens would have compressed further given more time.

We arrived at use of the full width at half-maximum for the cartilage thickness by starting with the assumption that our signal acquisition is independent of position within the field of view. We therefore convoluted a hypothetical rectangular object in frequency space with various passive filter functions putatively representing the effect of our measurement system (including rotations of the rectangular object that correspond to the cartilage tilt) and found that the signal intensity at the positions corresponded to the edges of the initial box function always contained the value of half the maximum height of the resulting curve.

Given that we have deduced the cartilage thickness at 5-second intervals during the deformation creep experiment, we calculated strain at each of these time points, defined as the fractional change in thickness of the cartilage from its initial non-compressed state as described by Eq. [4]

$$e_i = \frac{L_i - L_0}{L_0} \tag{4}$$

where e_i is strain at time i, L_i is cartilage thickness at time i, and L_0 is the initial cartilage thickness.

In doing so, we obtained the deformation creep curves shown in Fig. 3, which are similar to those found in

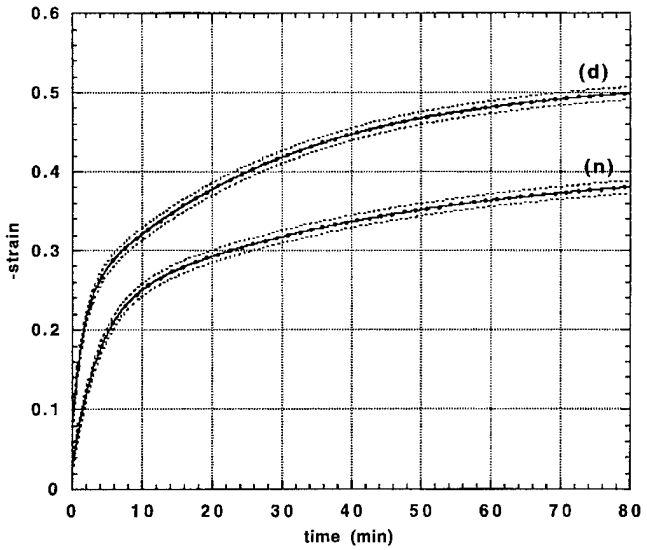

Figure 3. Deformation creep curve of normal and degraded cartilage specimens. Strain, defined as the fractional change in cartilage thickness resulting from a constant pressure application of 0.690 MPa, is shown as a function of time. The solid lines represent biexponential least squares fit to the cartilage thickness calculations, represented as circles. The curve for the normal cartilage specimen is labeled n, and the curve corresponding to the trypsin-degraded cartilage specimen is labeled d. The standard deviations of strain measurements are shown as dotted lines.

previous purely mechanical studies (17,18). Most notably, Mow et al (18) observed a 15% strain for an applied pressure of 0.1 MPa. The shape of the creep curve generated in Mow et al's experiment is similar to the shape we obtained and has a similar time constant. We have fit these curves to a general exponential decay function given by Eq. [5],

$$e = m_1\left(1 - \exp\left(-\frac{t}{m_2}\right)\right) + m_4\left(1 - \exp\left(-\frac{t}{m_5}\right)\right) + m_3 \quad (5)$$

where e is strain, t is time, and (m_1, m_2, m_3, m_4, m_5) are fit parameters. Two time constants were required for an adequate fit. The least squares fit results are given in Table 1.

Effects of Compression on Imaging Parameters

Spin-lattice, T1, and spin-spin, T2 magnetic resonance relaxation time constant maps were generated from a series of slice-selective spin-echo images acquired both before and after compression of the cartilage. As discussed in the methods section, these measurements of T1 and T2 are used for comparative purposes. The values reported may contain inaccuracies since the measurement methods were non-standard and were not calibrated. These maps, along with proton density-weighted images, are shown in Fig. 4 for representative normal and trypsin-degraded cartilage specimens. In the cases of both normal and degraded cartilage specimens, the proton density-weighted images displayed a fairly uniform image intensity prior to and subsequent to compression. In contrast, the relaxation time maps had a uniform intensity only after compression. Prior to compression, T1 was fairly heterogeneous throughout the imaging slice, and high values of T2 were predominantly located in the region of the articular surface in both the normal and trypsin-degraded cases.

Since the relaxation time constants throughout the imaging slice of the cartilage specimens were not uniform prior to compression, we have calculated T1 and T2 histograms of the normal and degraded cartilage specimens prior to and after compression. T1 histograms for both specimens before and after compression are shown in Fig. 5. We should note that experimental factors could have contributed to the relaxation time distributions. For example, the width of the T1 histogram could represent noise in the T1 map rather than an actual T1 distribution, especially since T1 in cartilage has been shown to be relatively homogeneous (19). When testing this notion by evaluating the pixel-by-pixel reproducibility of T1 maps of cartilage specimens and agarose phantoms, we found relatively little consistency. However, the fact that the T1 distribution narrows upon compression could implicate the existence of T1 heterogeneity. Although there was a reduction in T1 for both specimens upon compression, the change in T1 for the degraded specimen, upon compression, was substantially more dramatic than that corresponding to the normal specimen.

T2 histograms for both specimens before and after compression are shown in Fig. 6. Unlike the case for T1, the reductions in T2 for both the normal and degraded specimens were similar. However, T2 measurements for the degraded specimen both before and after compression were slightly higher than those for the normal specimen. As is indicated in the images of Fig. 4, the histograms of Figs. 5 and 6 likewise indicate that both relaxation time constants become more uniform upon compression for normal and degraded cartilage.

From the T1 and T2 histograms, we have calculated average values of T1 and T2 prior to and after compression for both the normal and degraded specimens. These values are given in Table 2.

Table 1
Deformation Creep Curves Fit to a Biexponential Decay*

	Normal specimen	Degraded specimen
m_1	0.18397	0.27486
m_2	43.256	29.206
m_3	0.030851	0.080153
m_4	0.19517	0.16205
m_5	3.7087	1.5768

*The deformation creep data of Fig. 3 were fit to the biexponential decay function given in Eq. [5].

Permeability Calculation

The data from the deformation creep experiment permits us to calculate the permeability of the cartilage assuming that the deformations are within the elastic limit. The most direct approach to calculating permeability within this experimental context is to use Darcy's law, which states that the velocity of the fluid in a permeable solid matrix is linearly proportional to the pressure gradient (17). The permeability of the matrix, k, is defined as the constant of proportionality. This

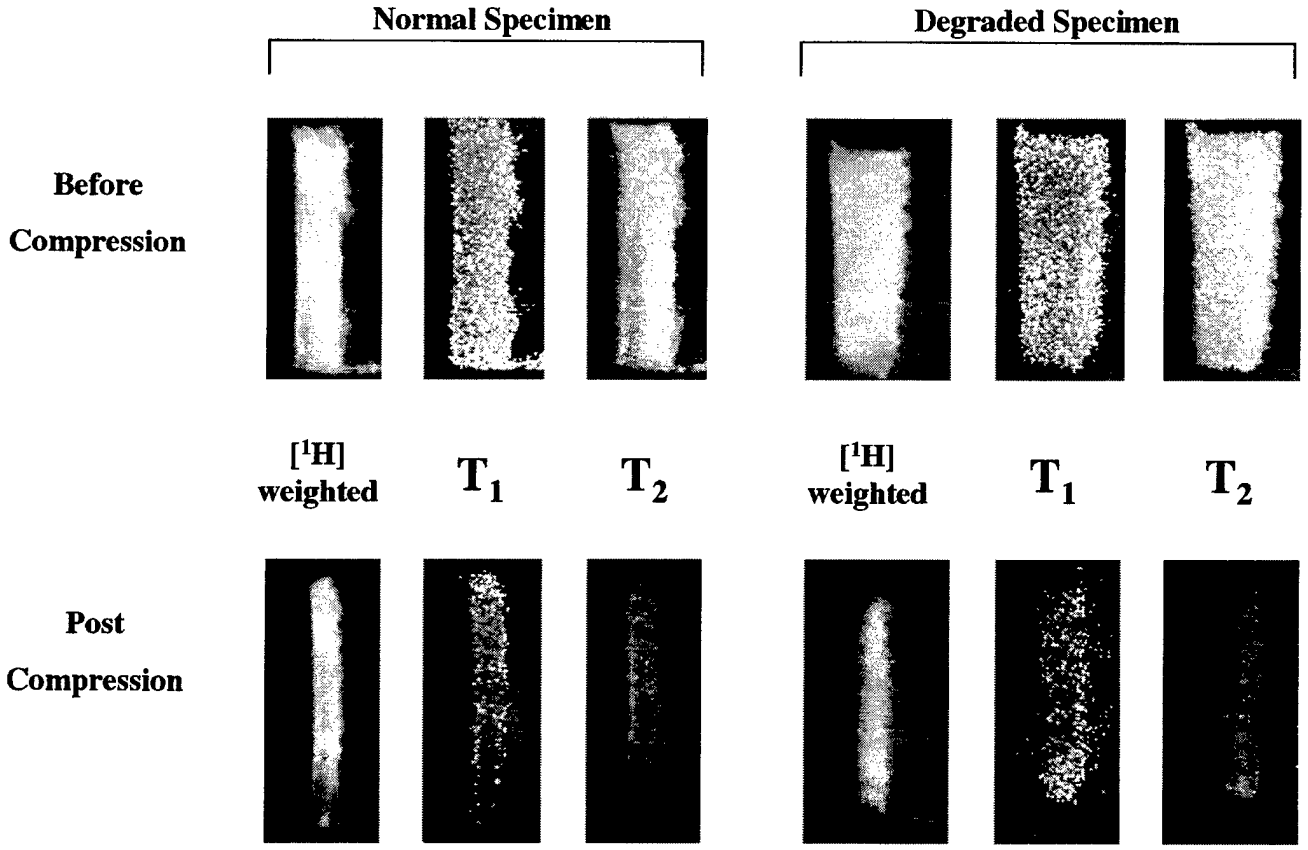

Figure 4. Images and relaxation time maps of normal and trypsin-degraded cartilage specimens. Each slice is along a diameter of the cartilage specimen. The left side of each image corresponds the region of cartilage adjacent to the ceramic piston of the pressure cell. The right side of each image corresponds to the articular surface of the cartilage adjacent to the glass filter. Image intensities of the normal and degraded spin-echo images are shown with the same image intensity scaling before and after compression, respectively. All T1 maps have the same scaling, and likewise, all T2 maps have the same scaling.

relationship is expressed symbolically in Eq. [6].

$$\mathbf{v} = k\nabla p \tag{6}$$

where $\mathbf{v}$ is the velocity, and p is the pressure. All three variables in this relationship are assumed to be functions of both space and time.

Since our experimental setup is designed to study the deformation of cartilage in one dimension (ie, the cartilage is confined such that it cannot expand laterally), we can treat Eq. [6] in a one-dimensional fashion where x is position. Since our experiment collects data at discrete time points, it is useful to include time explicitly in a discrete fashion, as indicated by Eq. [7] where the subscript i indicates a particular point in time:

$$k_i = \frac{v_i}{\left(\frac{dp}{dx}\right)_i}. \tag{7}$$

It will be useful to express Eq. [7] completely in terms of parameters derived directly from a deformation creep experiment, namely, L_0, the original thickness of the cartilage; P, the constant pressure applied to the cartilage; L_f, the equilibrium thickness of the cartilage under pressure P; Δt, the time step between each data acquisition; and e_i, the strain at time step i.

Since the fluid can be considered incompressible for our purposes, for the sake of simplicity, we make the approximation that the velocity of the fluid at all points within the cartilage is uniform and can be expressed as

$$v_i = \frac{\Delta L_i}{\Delta t} \tag{8}$$

where

$$\Delta L_i = L_i - L_{i-1} \tag{9}$$

and L_i is the thickness of the cartilage at time i. Furthermore, since our working definition of strain is

$$e_i = \frac{L_i - L_0}{L_0} \tag{10}$$

a substitution of Eq. [10] into Eq. [8] yields an explicit expression for v_i

$$v_i = \frac{L_0 \Delta e_i}{\Delta t} \tag{11}$$

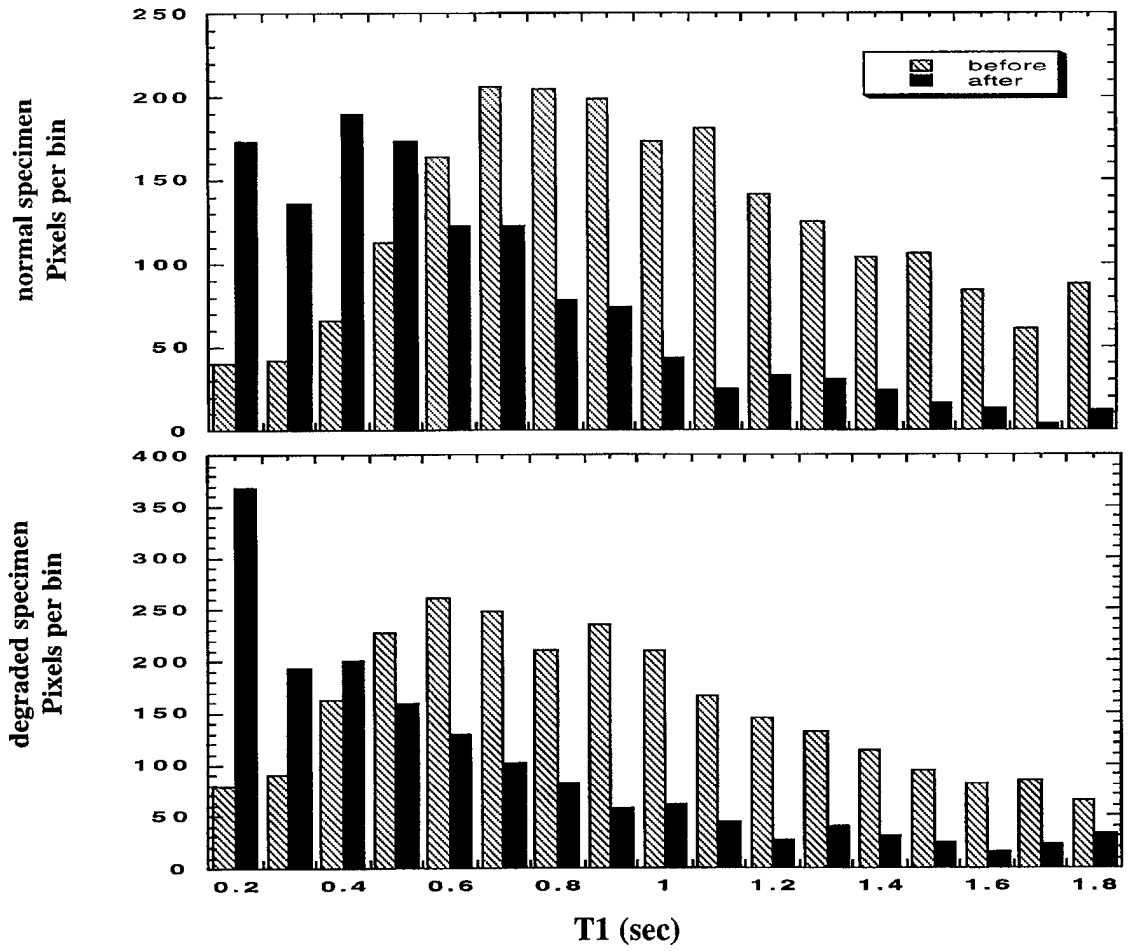

Figure 5. Apparent spin-lattice relaxation time constant, T1, histograms of the normal and degraded cartilage specimens both before and after compression.

where

$$\Delta e_i = e_i - e_{i-1}. \tag{12}$$

Let us assume for simplicity that the elastic properties of the cartilage specimen are homogeneous. With this assumption, and since there are no pressure sources or sinks within the cartilage volume, the pressure gradient throughout the cartilage volume is constant. Thus, the pressure can be expressed as a linear function of space

$$p = Ax + B \tag{13}$$

where A and B are defined by the boundary conditions. Not all of this pressure, however, affects the velocity of the interstitial fluid, since a portion, p_e, is absorbed by the elastic resistance of the cartilage

$$p_e = Ee \tag{14}$$

where E is the elastic modulus of the cartilage. The change in pressure across the thickness of the cartilage is thus

$$\Delta p = P - p_e = P - Ee \tag{15}$$

where P is the constant applied pressure. The elastic modulus, E, of the cartilage can be defined by the equilibrium strain for a given pressure

$$E = \frac{P}{(L_f - L_0)/L_0}. \tag{16}$$

Substituting Eq. [16] into Eq. [15] and dividing by the thickness of the cartilage at time i leads to the uniform pressure gradient, given by

$$\left(\frac{dp}{dx}\right)_i = (P/L_i)\left(1 - \frac{e_i L_0}{(L_f - L_0)}\right). \tag{17}$$

Substituting Eqs. [17] and [11] into Eq. [7], we obtain an explicit expression for permeability in experimentally derived terms

$$k_i = \frac{L_0 \Delta e_i}{\left(\frac{P\Delta t}{L_i}\right)\left(1 - \frac{e_i L_0}{(L_f - L_0)}\right)}. \tag{18}$$

The biexponential fits to the deformation creep data, when substituted into Eq. [18], provide the plots of permeability as a function of strain given in Fig. 7. The figure indicates that, in the uncompressed state, the trypsin-degraded specimen is approximately twice as

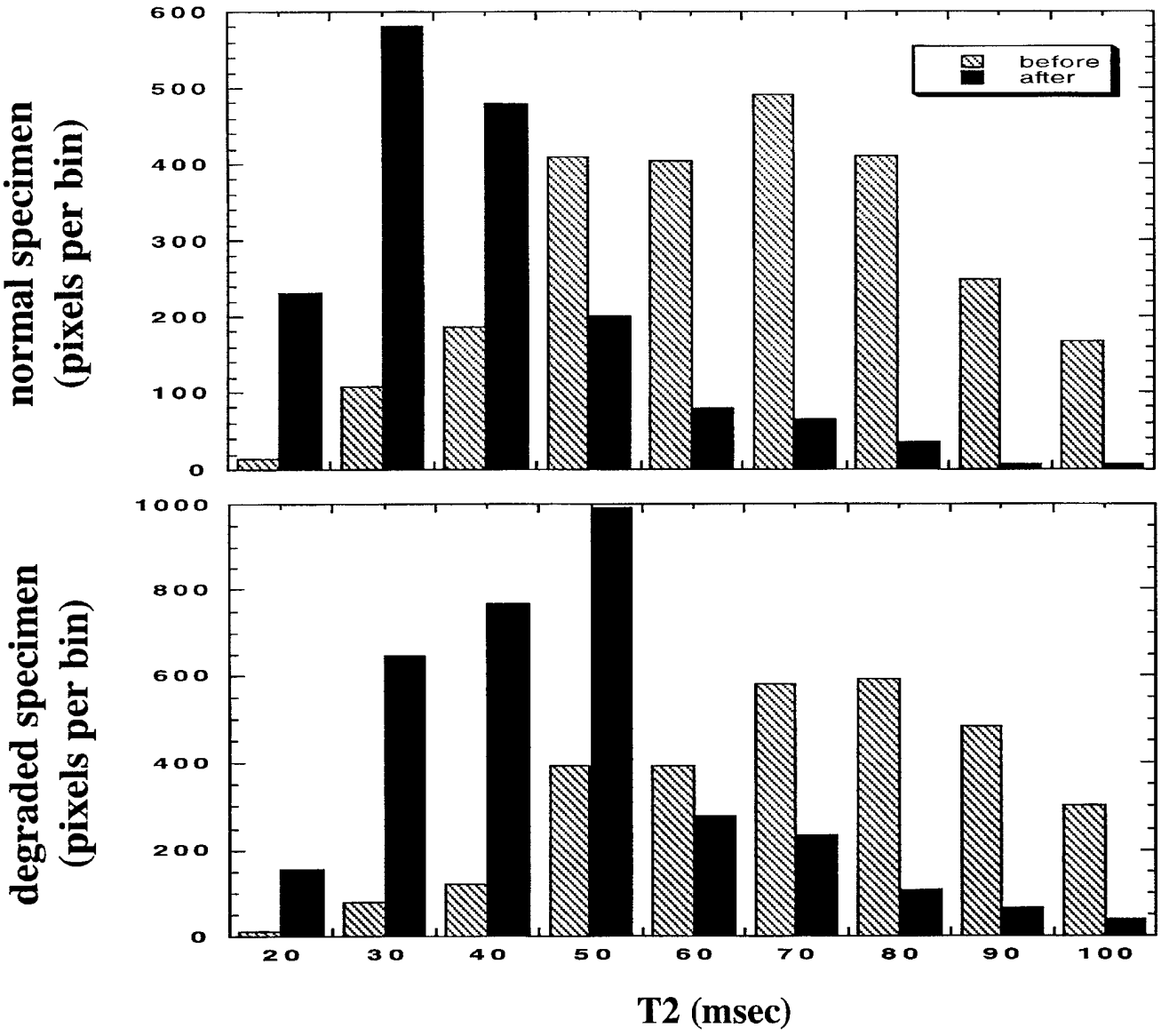

Figure 6. Apparent spin-spin relaxation time constant, T2, histograms of the normal and degraded cartilage specimens both before and after compression.

permeable to the normal specimen and that the increase in permeability with respect to strain is sharper than that of the normal specimen. The permeability of the specimen in the region of high strain (greater than 0.3) is unlikely to be accurately represented by this method since the fluid velocity in this range becomes small. Additionally, in the region of high strain, our experimental conditions exceed the elastic limit for articular cartilage as reported by Mow et al (18). Figure 8 shows the permeability, calculated in the same manner, as a function of time for the deformation of both the normal and degraded specimen. This figure shows that during the course of deformation, the degraded specimen is initially more permeable than the normal specimen, but after approximately 5 minutes of sustained compression, the degraded specimen loses its permeability with respect to the normal specimen.

Table 2
Changes in Apparent Relaxation Parameters With Compression*

	T1 (sec)	T2 (msec)
Normal before	0.99 ± 0.38	66.4 ± 47.2
Normal after	0.62 ± 0.55	38.4 ± 35.6
Degraded before	0.91 ± 0.36	71.9 ± 46.5
Degraded after	0.60 ± 0.57	46.9 ± 39.7

*The averages of spin-latice (T1) and spin-spin (T2) relaxation time constants were calculated from the maps shown in Fig. 4.

DISCUSSION

MR Properties

The experiments described in this manuscript expand on earlier progress to identify early manifestations of osteoarthritis using MR imaging such as observations of MR signal intensity changes across the depth of the cartilage (20) and measurements of MR relaxation time constants of normal and degraded cartilage (21). MR relaxation times have also previously been observed to change in a depth-dependent fashion in normal articular cartilage specimens during compression (22). Our

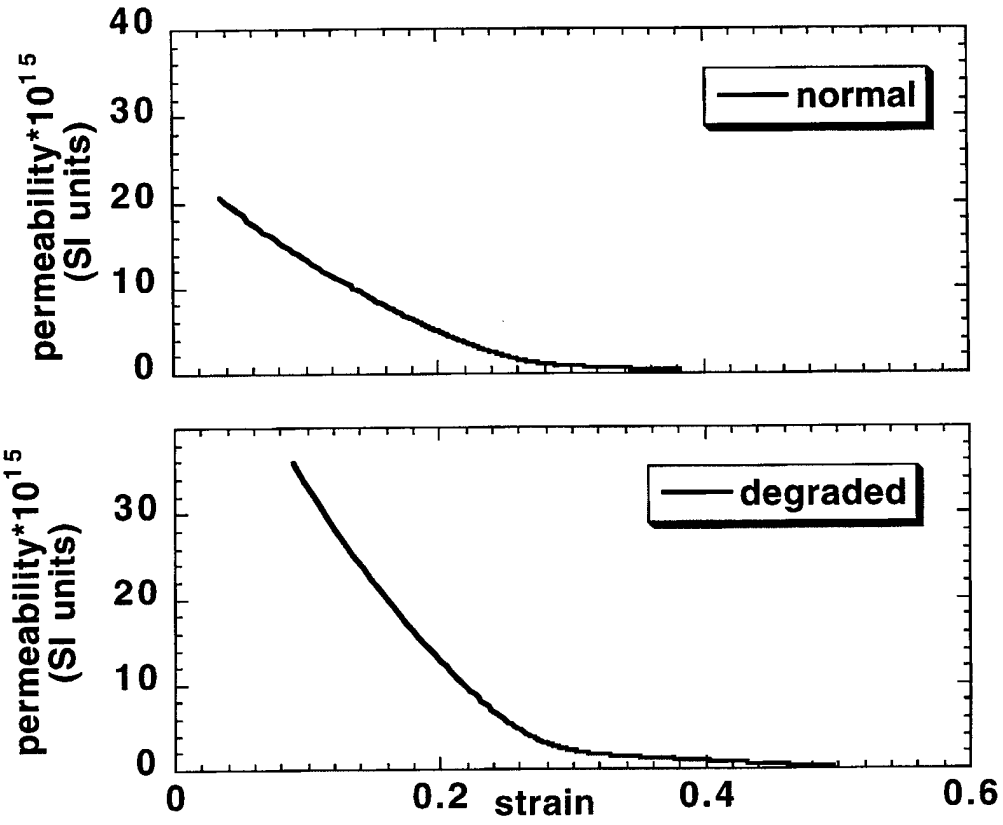

Figure 7. Permeability of the normal and degraded cartilage specimens as a function of strain, defined as the absolute value of the fractional change in cartilage thickness during compression.

present observations of the MR properties of bovine specimens of articular cartilage are consistent with these previous studies. However, we were unable to observe consistent depth-dependent results with all specimens. This inconsistency could result from the likelihood that juvenile cartilage specimens (which we used) are likely to be structurally distinct from adult cartilage (3). In addition, with our technique, it was difficult to assess the MR characteristics of the cartilage at the articular surface since some imaging artifacts did arise from the interface of the cartilage with the glass filter.

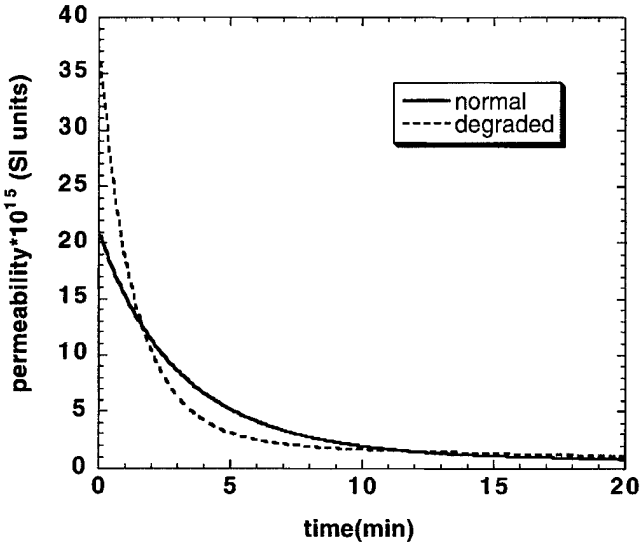

Figure 8. Permeability of the normal and degraded cartilage specimens as a function of time.

Viscoelastic Properties

There are a multitude of theories describing the mechanical properties of articular cartilage, including the electrostatic interactions among negatively charged proteoglycans (23), the viscous interaction between the cartilage fluid and its solid matrix (11), and the microstructural organization of cartilage (24). It has been proposed that purely viscoelastic models of articular cartilage may not be adequate for a comprehensive treatment of the mechanical properties of cartilage (25). However, the distinction between poroelastic and viscoelastic deformations could be a matter of semantics. Viscoelastic models are found to be consistent with numerous experimental observations (26).

We chose to apply a simple rheological model to our data and expand it as necessary. Since the data from our deformation creep experiment at first glance approximate a function that exponentially rises to a fixed value, we chose the Voigt (15) viscoelastic model shown in Fig. 9, which is described by Eq. [19].

$$e = \frac{P}{E}\left(1 - \exp\left(-\frac{E}{v}\right)\right) + c \qquad (19)$$

where e is strain, P is pressure, E is the elastic modulus, v is the viscosity, and c is an arbitrary constant. However, we found that two time constants were necessary for an adequate fit to our observations. Thus, the

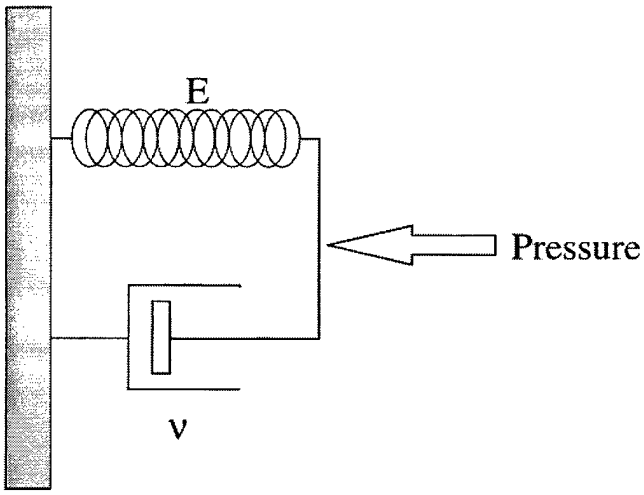

Figure 9. Voigt viscoelastic model. This basic viscoelastic model consists of an elastic spring arranged in parallel to a viscous dashpot. As indicated, E is the elastic modulus, and v is the viscosity.

mathematical description of two Voigt solids in series adequately fit the data as shown in Fig. 3.

Our experiment was designed to mimic physiological pressures that are well beyond the elastic limit of cartilage, which does place limits on the present physical interpretation of a viscoelastic model. However, we can state that the deformation creep observations are consistent with the notion that the cartilage rheology can be described by a linked deformation of two components.

In general the observed changes in permeability and elastic moduli resulting from degradation are consistent with mechanical studies involving alternative arthritic models, such as a canine surgically induced arthritic model (27), as well as other enzymatic degradation models (28). Furthermore, our observations that permeability increases with trypsin digestion is consistent with the notion that a reduction in fixed charge density within the cartilage matrix induces an increase in permeability (29). We have described an approach to investigating cartilage functionality in vitro that could lend insight into the design of experiments in vivo. Furthermore, the degree of consistency between the experimental results and a two time constant viscoelastic model lends credence to the notion that the histological zones of articular cartilage have distinct mechanical properties.

REFERENCES

1. Hamerman D. The biology of osteoarthritis. N Engl J Med 1989;320: 1322–1330.
2. Recht MP, Resnick D. MR imaging of articular cartilage: current status and future directions. AJR 1994;103:283–290.
3. Torzilli PA. Water content and equilibrium water partition in immature cartilage. J Orthop Res 1988;6:766–769.
4. Hall AC, Horwitz ER, Wilkins RJ. The cellular physiology of articular cartilage. Exp Physiol 1996;81:535–545.
5. Donnan FG. The theory of membrane equilibria. Chem Rev 1924;1: 73–90.
6. Khalsa PS, Eisenberg SR. Compressive behavior of articular cartilage is not completely explained by proteoglycan osmotic pressure. J Biomech 1997;30:589–594.
7. Maroudas A, Bayliss MT, Uchitel-Kaushansky N, Schneiderman R. Aggrecan turnover in human articular cartilage: use of aspartic acid racemization as a marker of molecular age. Arch Biochem Biophys 1998;350:61–71.
8. Platt D, Bird JL, Bayliss MT. Ageing of equine articular cartilage: structure and composition of aggrecan and decorin. Equine Vet J 1998;30:43–52.
9. Wei L, Svensson O, Hjerpe A. Correlation of morphologic and biochemical changes in the natural history of spontaneous osteoarthrosis in guinea pigs. Arthritis Rheum 1997;40:2075–2083.
10. McCutchin CW. The frictional properties of animal joints. Wear 1972;5:1–17.
11. Mow VC, Holmes MH, Lai WM. Fluid transport and mechanical properties of articular cartilage: a review. J Biomech 1984;17:377–394.
12. Neeman M, Freyer JP, Sillerud LO. Pulsed-gradient spin-echo diffusion studies in NMR imaging. Effects of the imaging gradients on the determination of diffusion coefficients. J Magn Reson 1990; 90:303–312.
13. Brandl M, Haase A. Molecular diffusion in NMR microscopy. J Magn Reson B 1994;103:162–167.
14. Carr HY, Purcell EM. Effects of diffusion on free precession in nuclear magnetic resonance experiments. Phys Rev 1954;94:630–635.
15. Fung YC. The foundations of solid mechanics. Englewood Cliffs, NJ: Prentice Hall; 1965. p 22.
16. Mow VC, Hou JS, Owens JM, Ratcliffe A. Biphasic and quasilinear viscoelastic theories for hydrated soft tissues. In: Mow VC, Ratcliffe A, Woo SL, editors. Biomechanics of diarthrodial joints, vol. One. New York: Springer Verlag; 1990.
17. Mansour JM, Mow VC. The permeability of articular cartilage under compressive strain and at high pressures. J Bone Joint Surg 1976;58A:505–516.
18. Mow VC, Kuei SC, Armstrong CG. Biphasic creep and stress relaxation of articular cartilage in compression: theory and experiments. J Biomech Eng 1980;102:73–84.
19. Xia Y. Relaxation anisotropy in cartilage by NMR microscopy (μMRI) at 14 μM resolution. Magn Reson Med 1998;39:941–949.
20. Paul PK, Jasani MK, Sebok D, Rakhit A, Dunton AW, Douglas FL. Variation in MR signal intensity across normal human knee cartilage. J Magn Reson Imaging 1993;3:569–574.
21. Lehner KB, Rechl HP, Gmeinwieser JK, Heuck AF, Lukas HP, Kohl HP. Structure, function, and degeneration of bovine hyaline cartilage: assessment with MR imaging in vitro. Radiology 1989;170:495–499.
22. Rubenstein JD, Kim JK, Henkelman RM. Effects of compression and recovery on bovine articular cartilage: appearance on MR images. Radiology 1996;201:843–850.
23. Buschmann MD, Grodzinsky AJ. A molecular model of proteoglycan-associated electrostatic forces in cartilage mechanics. J Biomech Eng 1995;117:179–192.
24. Schwartz MH, Leo PH, Lewis JL. A microstructural model for the elastic response of articular cartilage. J Biomech 1994;27:865–873.
25. McCutchen CW. Cartilage is poroelastic, not viscoelastic (including an exact theorem about strain energy and viscous loss, and an order of magnitude relation for equilibration time). J Biomech 1982;15:325–327.
26. Kovach IS. A molecular theory of cartilage viscoelasticity. Biophys Chem 1996;59:61–73.
27. Setton LA, Mow VC, Muller FJ, Pita JC, Howell DS. Mechanical properties of canine articular cartilage are significantly altered following transection of the anterior cruciate ligament. J Orthop Res 1994;12:451–463.
28. Bader DL, Kempson GE. The short-term compressive properties of adult human articular cartilage. Bio-Med Materials Eng 1994;4:245–256.
29. Gu WY, Lai WM, Mow VC. Transport of fluid and ions through a porous-permeable charged-hydrated tissue, and streaming potential data on normal bovine articular cartilage. J Biomech 1993;26: 709–723.

Original Research

Sodium and Proton MR Properties of Cartilage During Compression

Ravinder Reddy Regatte, PhD,* Jonathan H. Kaufman, MS, Elizabeth A. Noyszewski, PhD, and Ravinder Reddy, PhD

Proton and sodium MR relaxation times of bovine articular cartilage specimens were measured as a function of proteoglycan (PG) depletion and as a function of mechanical compression. Proton and sodium relaxation times of normal cartilage were compared with relaxation times of PG-depleted cartilage to evaluate the significance of PG depletion-induced changes in MR relaxation parameters. These comparisons were conducted for both uncompressed and mechanically compressed states. The mechanical compressions were performed with an MR-compatible pressure cell and evaluated dynamically via interleaved one-dimensional proton and sodium MR projection imaging. The comparisons indicate that sodium relaxation parameters are sensitive to PG depletion when cartilage is in a mechanically compressed state or an uncompressed state. In contrast, proton relaxation parameters do not change significantly with PG depletion when cartilage is in an uncompressed state. However, during mechanical compression, proton T2 becomes sensitive to PG depletion. These results support the potential of sodium magnetic resonance imaging (MRI) as a possible modality for obtaining imaging contrast related to PG depletion. The results also indicate the potential of proton MRI to provide such contrast if the image acquisition is conducted in conjunction with a mechanical compression via physical exercise. J. Magn. Reson Imaging 10:961–967, 1999.

Index terms: cartilage; compression; NMR; relaxation; sodium; proteolysis

ARTICULAR CARTILAGE is a dense connective tissue composed primarily of water, collagen fiber bundles, and proteoglycan aggregates. Cartilage functions as the load-bearing surface of all synovial joints. The normal function of articular cartilage involves compression. As cartilage is compressed, the fluid contained within the matrix is extruded into the joint space. This extruded fluid acts as a lubricant between the contact points of opposing bone interfaces (1). The disease process of osteoarthritis (OA) involves the degeneration of articular cartilage. The earliest putative changes in cartilage due to OA are a) softening of cartilage, b) a decrease in proteoglycan content, c) an increase in water content, d) changes in cartilage thickness, and e) an increase in permeability (2–5). Each of these changes has been associated with an alteration in the mechanical properties of cartilage (6–8). Therefore, there has been substantial interest in studying the mechanical properties of normal and degenerated articular cartilage.

Several investigators have used proton MRI to observe cartilage image dynamics during compression (9,10). However, they could only report qualitative effects because MR relaxation time constants were not measured. Previously, we have estimated the relative changes in proton MR relaxation parameters of articular cartilage specimens as a function of compression (11). This previous work indicated that both proton T1 and T2 decrease with compression. However, this indication was based on non-standard methods for measuring relaxation parameters. In the present work we use standard inversion recovery and Hahn spin-echo techniques to obtain robust values for proton relaxation parameters of cartilage during mechanical compression.

In addition to proton, sodium is an important nucleus in cartilage physiology. Several investigators have measured the MR properties of sodium as a function of cartilage degeneration (3,12–15). Such studies with sodium have yet to incorporate the effects of mechanical compression. Therefore, in addition to the proton measurements, we have extended the objective of the present study to obtain measurements of sodium relaxation parameters as a function of compression. In both cases, we examined the effects of enzymatic proteoglycan depletion on the observed compression-induced trends in relaxation times.

MATERIALS AND METHODS

Cartilage Specimens

Ten 1-cm-diameter cylindrical cartilage plugs were harvested, each from the flat surface of a bovine patella. All patellae were stored at 20°C prior to the experiment. It is unknown what the effect of freezing is on cartilage specimens. Each cartilage specimen was sectioned with a diamond core drill and then peeled from the cartilage-

MMRRCC, Department of Radiology, University of Pennsylvania Medical Center, Philadelphia, Pennsylvania, 19104-6100.

Contract grant sponsor: NIH; Contract grant numbers: RR02305, RO1 AR45242-01, and R01-AR45404; Contract grant sponsor: GE Research Fund.

*Address reprint requests to: R.R.R., MMRRCC, Department of Radiology, University of Pennsylvania Medical Center, 422 Curie Blvd, B1 Stellar-Chance Labs, Philadelphia, PA, 19104-6100.

February 1, 1999;July 13, 1999

bone interface with a spatula. The specimens were subsequently inspected to ensure that there was no visible damage and that all cartilage layers remained intact. Each specimen was equilibrated in phosphate-buffered saline, pH 7.4 (Sigma, St. Louis, MO) for 30 minutes.

Five of the cartilage specimens were exposed to enzymatic digestion. Since it has been hypothesized that early stages of OA involve the selective loss of proteoglycan (PG) content, we chose a proteolytic agent that would deplete the proteoglycan content of the cartilage while leaving the collagen network relatively intact. The digested cartilage specimens were generated by incubating each cartilage specimen in 5 ml of 1.0 mg trypsin/ml phosphate-buffered saline solution (Sigma) for 60 minutes. The end-stage digestion medium was analyzed for proteoglycan content via a spectrophotometric assay (16). In each case, the PG concentration in the media was approximately 1.3 mg/ml, which corresponds to an approximate 30% PG depletion.

Pressure Cell Design and Construction

The pressure cell consists of a pneumatically activated ceramic piston and porous glass filter in a cylindrical Delrin chamber, as shown in Fig. 1. The details of the pressure cell are given elsewhere (11). Each cartilage plug was placed between the piston and filter such that the articular surface of the cartilage was adjacent to the porous glass filter. The pressure cell was oriented such that the cartilage articular surface was parallel to the main magnetic field (B_0). The ceramic piston compressed each cartilage specimen, while the porous glass filter allowed the extrusion of cartilage fluid. A double-tuned solenoid radiofrequency (RF) coil was incorporated into the pressure cell. The transmit/receive solenoidal RF coil was double-tuned to the Larmor frequencies of H-1 (86.1 MHz) and Na-23 (22.7 MHz) as described by Schnall et al (17). The pressure cell was placed inside an 11-cm-diameter local gradient set capable of generating 8 G/cm. The cell and gradient set were then placed in the center of a 2 T-Oxford whole-body imaging magnet interfaced to custom-built NMR spectrometer. The pressure cell was activated pneumatically, via a regulated (0.69 MPa) compressed air source. The pressure was measured at the source with a digital pressure gauge (Omega DPG-500).

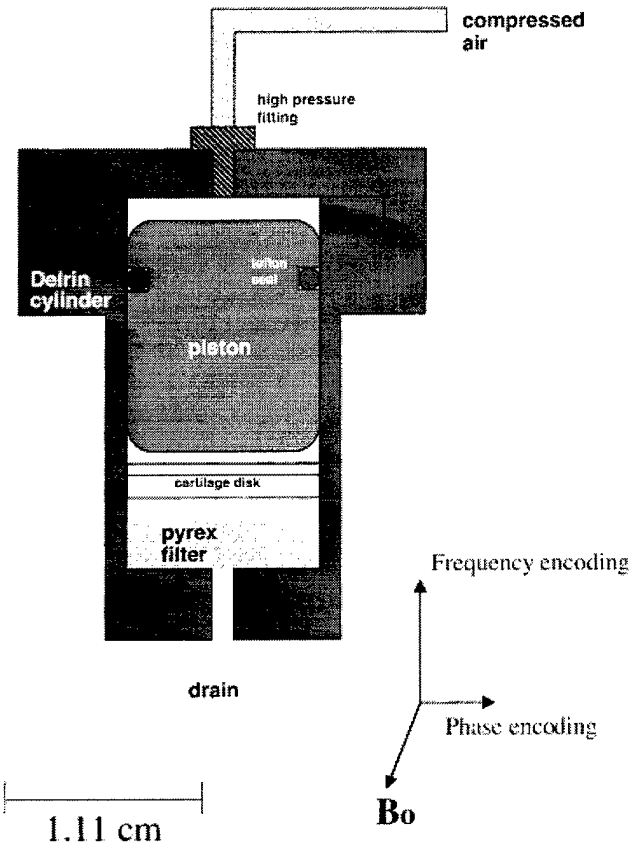

Figure 1. Cross-sectional diagram of MR-compatible pressure cell. Compressed air exerts a pressure on a piston that is confined in a cylindrical shaft. The piston, when responding to the pressure from the compressed air, pushes on the specimen that is positioned between the cylinder and a Pyrex filter, which allows cartilage fluid to extrude from the cell.

Proton and Sodium Relaxation Time Measurements

The standard inversion recovery technique was employed to obtain proton T1 measurements. For normal cartilage specimens, the inversion time was varied by step times of 200 msec before compression and 100 msec during compression. For the PG-depleted cartilage specimens, the inversion time varied by step times of 250 msec before compression and 125 msec during compression. In each case 30 free induction decays (FIDs) were acquired. Each FID contained 1024 data points at a sampling rate of 0.1 msec.

To measure proton T2, the standard Hahn spin-echo technique (18) was employed. For normal cartilage, the echo time (tau) was varied by 25 msec before compression and 10 msec during compression. For PG-depleted cartilage, tau was varied by 20 msec before compression and 8 msec during compression. Spectra at 30 time points were acquired for each T2 measurement. For each time point, 200 FIDs were averaged to obtain a spectrum.

Although sodium exhibits bi-exponential T1 in biological tissues, due to the small difference between the two T1s, it is difficult to measure each independently. Therefore, measurements of sodium spin lattice relaxation time constants, T1, were carried out using the same standard inversion-recovery methods used for proton. However, since the T1 of sodium is several orders of magnitude shorter than that of proton, the inversion time was varied by a step time of 6 msec before compression and 3 msec during compression for both normal and PG-depleted cartilage specimens. Thirty inversion time points were acquired for each T1 measurement; 200 FIDs were acquired and averaged for each inversion time. Each FID contained 1024 data points at a sampling rate of 0.1 msec.

The transverse relaxation of sodium is bi-exponential and thus has two time constants: T2f and T2s. It has been shown, using triple quantum filtered spectra, that

only the slow component, T2s, is sensitive to compression (19). Therefore we used the same standard Hahn spin-echo technique for the measurement of sodium transverse relaxation times as was used as in the case for proton transverse relaxation times. For normal cartilage, tau was varied by 4 msec before compression and 2 msec during compression. For PG-depleted cartilage, tau was varied by 3 msec before compression and 1 msec during compression. Spectra at 30 time points were acquired for each T2 measurement. For each time point, 200 FIDs were averaged to obtain a spectrum.

Projection Images

One-dimensional proton and sodium projection images, in a direction perpendicular to the articular surface, were acquired with the pulsed gradient spin-echo pulse sequence (PGSE). The proton imaging parameters were as follows: TR 1 second, TE 20 msec, number of excitations (NEX) 1. For sodium projections, the imaging parameters were as follows: TR 100 msec, TE 3 msec, NEX 800. The acquisitions of proton and sodium projection images were interleaved. The total acquisition time for one set of interleaved proton and sodium projection images was 81 seconds (1 second for the proton projection image and 80 seconds for the sodium projection image). One hundred interleaved projection images were collected for a total duration of approximately 135 minutes.

RESULTS

Demonstration of Compression

Figure 2 shows a series of one-dimensional proton projection images of cartilage acquired before and during the deformation. These projections were acquired every 81 seconds for a period of 135 minutes. The ceramic piston compressed the cartilage from the right side toward the filter on the left. The low-intensity plateau on the left side of the projection image corresponds to the position of the glass filter. The projection images narrow with the pressure onset, and the signal intensity drops as a function of time.

Figure 3 shows a series of one-dimensional sodium projection images of cartilage before and during deformation. As in the case of proton projections, the sodium projections were acquired every 81 seconds for a period of 135 minutes. With pressure application, the sodium projection images narrow, and sodium signal decreases.

Evidence of Enzymatic Induction of Cartilage Softening

Figure 4 shows the cartilage strain obtained from the proton and sodium projection images as a function of compression duration for both normal and PG-depleted cartilage. The strain calculations employed the consideration that the thickness of a cartilage specimen is approximately the full width at half maximum of the corresponding one-dimensional projection images shown in Figs. 2 and 3. The thickness calculation employed linear interpolation of signal intensity for

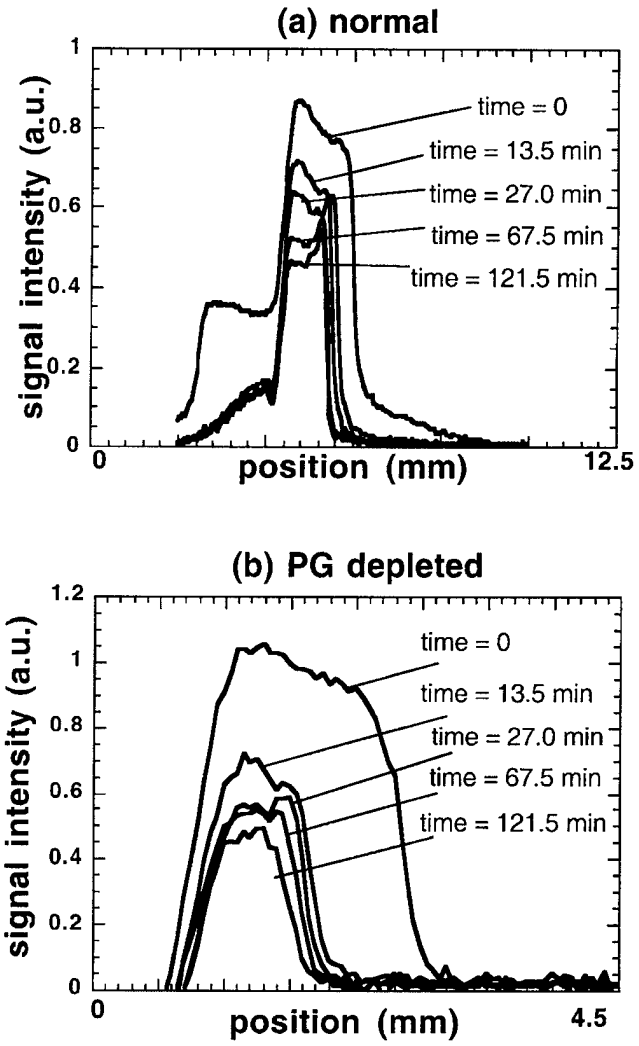

Figure 2. One-dimensional 90–180° spin-echo proton projection images of (**a**) a normal cartilage specimen, and (**b**) a PG-depleted cartilage specimen. Five projections are shown at various times after onset of pressure application. The compressive force is from right to left against the stationary glass filter. The left-hand slope of the projection corresponds to the articular surface of the cartilage specimen. The right-hand slope of the projection corresponds to the cartilage-bone boundary.

regions between those represented by pixels. Strain can be defined in the following three ways:

$$e = \frac{L_0 - L_1}{L_0}, \quad (1)$$

$$e = \frac{L_0 - L_1}{L_1}, \quad (2)$$

$$e = \frac{(L_0 - L_1)}{(1/2)(L_0 + L_1)}, \quad (3)$$

where L_0 is the original thickness, and L_1 is the thickness after compression. In this manuscript, we use the definition of strain expressed by Eq. [1]. Cartilage strain was evaluated at 81 second intervals.

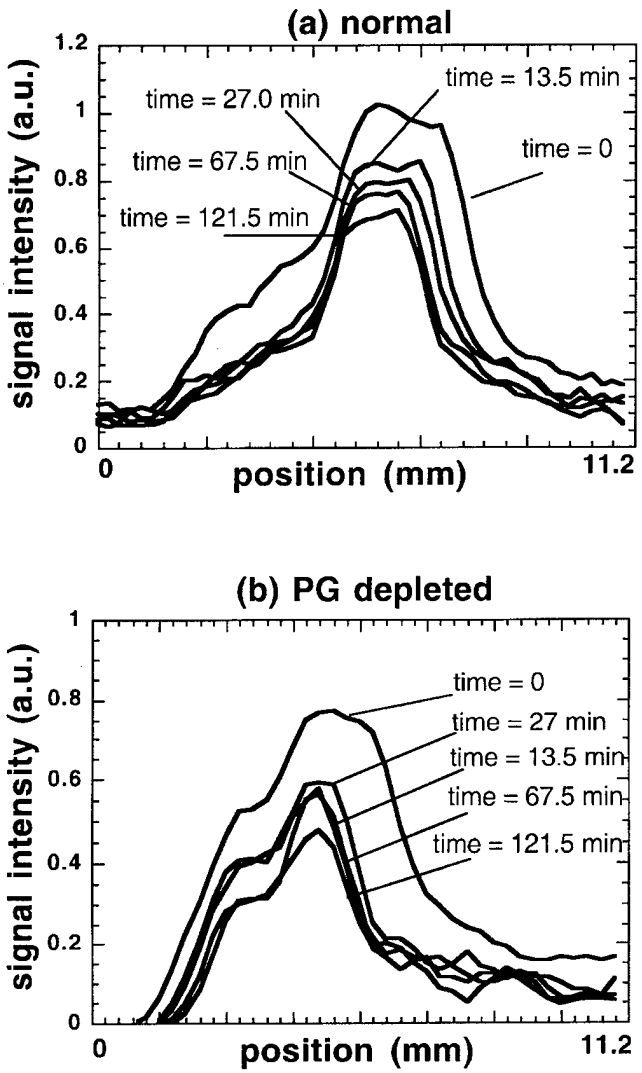

Figure 3. One-dimensional spin-echo sodium projection images of (**a**) a normal cartilage specimen, and (**b**) a PG-depleted cartilage specimen. Five projections are shown at indicated times after the onset of pressure application. The specimen orientation is identical to that of Fig. 2.

At the onset of pressure application, cartilage strain rapidly increased to a steady-state condition. The PG-depleted cartilage specimens were systematically more compliant than the normal specimens. The experimental creep data for both sodium and proton were fitted to a simple bi-exponential decay with two time constants given by

$$e = A_0 + A_1\left(1 - \exp\left(-\frac{t}{\theta_1}\right)\right) + A_2\left(1 - \exp\left(-\frac{t}{\theta_2}\right)\right) \quad (4)$$

where e is strain, t is time, and A_0, A_1, A_2, θ_1 and θ_2 are fit parameters (given in Table 1). This model mimics the mechanical processes of articular cartilage during confined compression as shown previously (11).

The shapes of the sodium and proton creep curves are similar. The PG-depleted specimens were almost twice as mechanically compliant as the normal specimens. The lower signal-to-noise ratios of the sodium projections compared with the proton projections is reflected as the large standard error of the sodium creep curves.

Effects of Compression on MR Relaxation Times

Figure 5 shows typical curve fits when calculating relaxation time constants. Table 2 presents a summary of the data obtained regarding the effects of compression and PG depletion on cartilage proton and sodium MR relaxation times. The four inherent parameters: proton-T1, proton-T2, sodium-T1, and sodium-T2 are delineated for the four physio-mechanical cartilage states: normal-uncompressed, normal-compressed, PG-depleted-uncompressed, and PG-depleted-compressed.

Each of the four parameters were evaluated, using a two-tailed *t*-test, to determine whether PG depletion had a significant effect on any of the MR time constants. The resulting *P* values are given in the last column of Table 2. In the uncompressed state, the sodium MR time constants show a much stronger PG depletion-induced distinction than do the proton MR time constants. There is no evidence that proton-T1 changes with PG depletion, and scarce evidence, if any, that proton-T2 changes. On the other hand, both sodium-T1 and sodium-T2 increase with PG depletion to a statistically significant extent.

Compressing cartilage provides a means of introducing a PG depletion-induced change in proton-T2. In the compressed state (using the same pressure), the proton-T2 of the PG-depleted cartilage is shorter than that of normal cartilage. Furthermore, the change in proton-T2 associated with compression is substantially more pronounced for PG-depleted cartilage than it is for normal cartilage.

The contribution of compression in distinguishing the effects of PG depletion on sodium MR relaxation parameters is less pronounced; the change in sodium-T2, associated with compression, is similar for the normal and PG-depleted specimens.

The data also provide an evaluation of the changes in proton and sodium relaxation time constants associated with compression. To compliment the values displayed in Table 2, we report the statistical significance of the compression-associated changes in relaxation time in Table 3.

DISCUSSION

The central aim of this study was to identify PG depletion-induced trends in proton and sodium MR relaxation times. These trends could serve as potential contrast mechanisms that indicate early cartilage degeneration and thus early signs of osteoarthritis. Since the normal functionality of articular cartilage involves compression, we have measured the MR relaxation times of articular cartilage in both uncompressed and mechanically compressed states. One motivation for the introduction of mechanical compression is that it has been

Figure 4. Typical relaxation time constant data fit to exponential functions: (**a**) proton T1, (**b**) sodium T1, (**c**, **d**) proton T2, and (**e**, **f**) sodium T2.

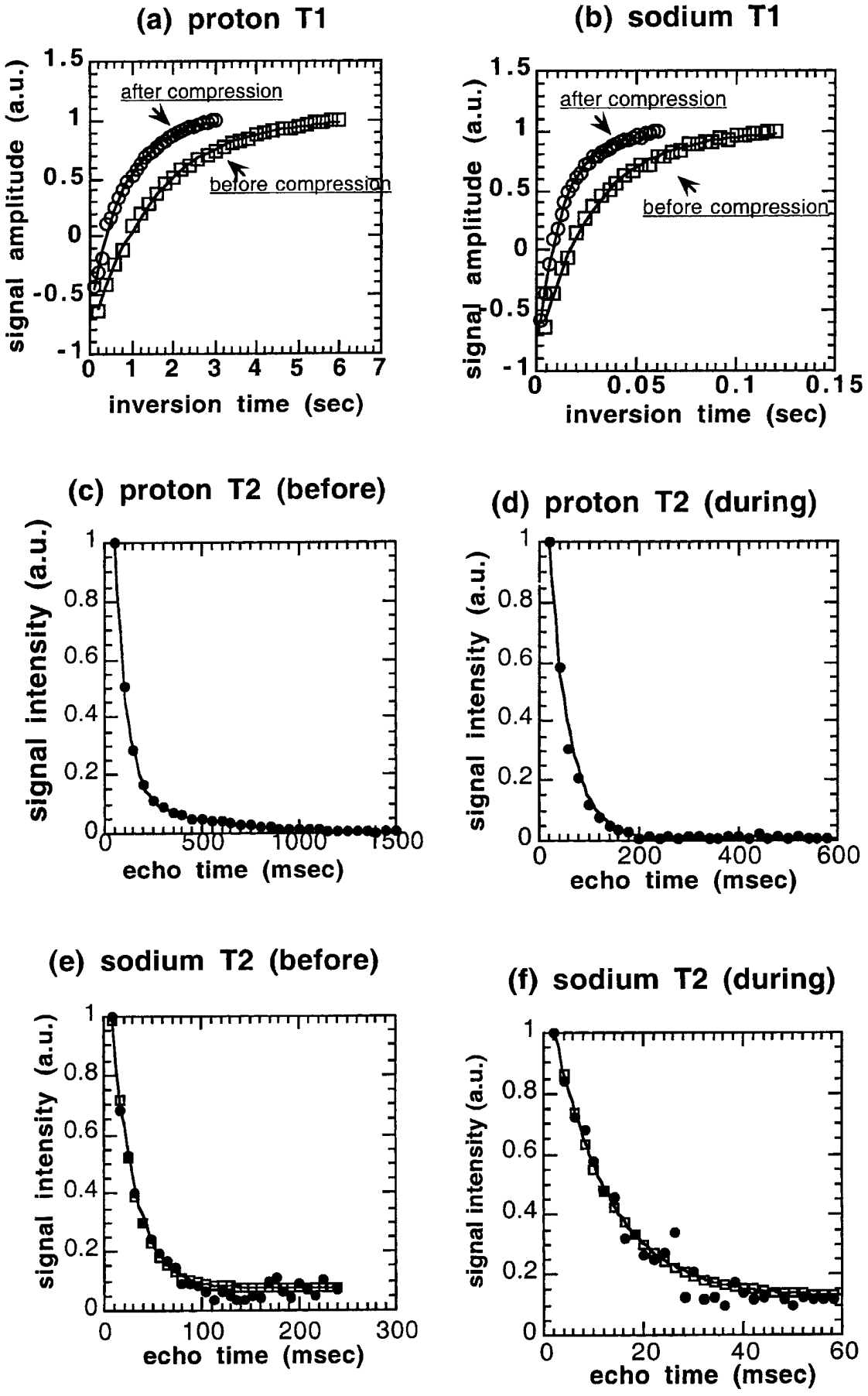
(a) proton T1
signal amplitude (a.u.)
1.5
1
0.5
0
-0.5
-1
after compression
before compression
0 1 2 3 4 5 6 7
inversion time (sec)
(b) sodium T1
signal amplitude (a.u.)
1.5
1
0.5
0
-0.5
-1
after compression
before compression
0 0.05 0.1 0.15
inversion time (sec)
(c) proton T2 (before)
signal intensity (a.u.)
1
0.8
0.6
0.4
0.2
0
0 500 1000 1500
echo time (msec)
(d) proton T2 (during)
signal intensity (a.u.)
1
0.8
0.6
0.4
0.2
0
0 200 400 600
echo time (msec)
(e) sodium T2 (before)
signal intensity (a.u.)
1
0.8
0.6
0.4
0.2
0
0 100 200 300
echo time (msec)
(f) sodium T2 (during)
signal intensity (a.u.)
1
0.8
0.6
0.4
0.2
0
0 20 40 60
echo time (msec)

Figure 4

Table 1
Deformation Creep Curve Fit Parameters of Fig. 4 Using Eq. [4]

Nucleus	PG depleted	A_0	A_1	A_2	θ_1	θ_2
Proton	No	0.0364	0.175	0.159	60.025	8.99
Proton	Yes	0.0385	0.127	0.127	18.153	28.09
Sodium	No	0.0046	0.157	0.155	8.182	54.042
Sodium	Yes	−0.1171	0.395	0.395	3.66	3.67

hypothesized that cartilage softening may be the earliest known indicator of osteoarthritis.

The method of this study employed one-dimensional projection imaging to monitor and verify cartilage compression. Furthermore, the degree of compression and the rate at which compression occurred for a given compressive load were calculated via the construction of deformation creep curves. These curves permitted

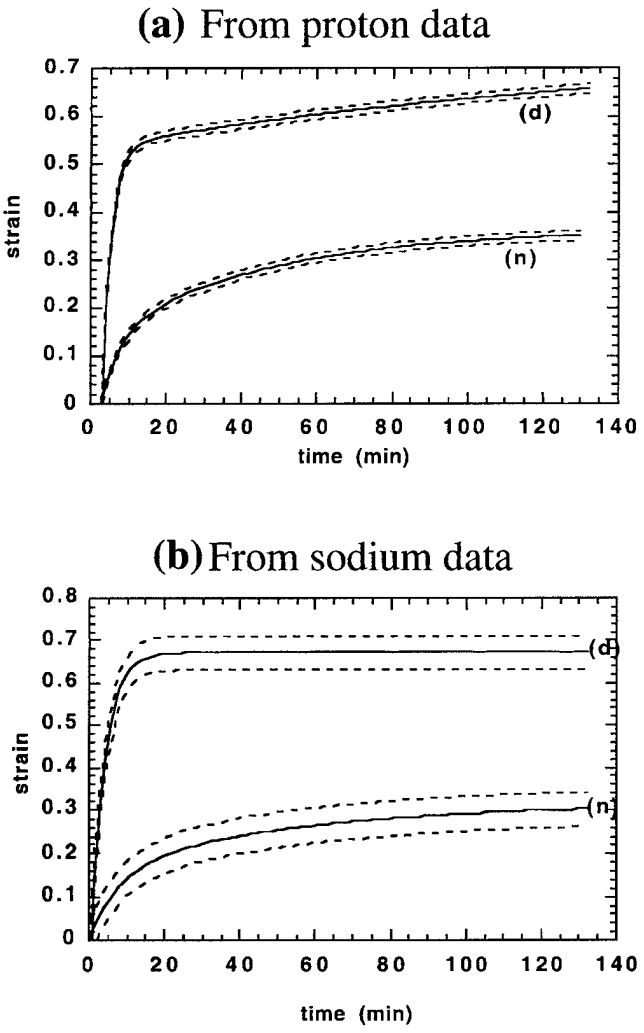

Figure 5. Deformation creep curve of a normal and a PG-depleted cartilage specimen obtained from proton and sodium projections. The curve for the normal cartilage specimen is labeled (n), and the curve corresponding to the PG-depleted cartilage specimen is labeled (d). The solid line represent bi-exponential least squares fits of the raw data to Eq. [4], and the dotted lines correspond to standard deviations of strain measurements.-

Table 2
Sodium and Proton Relaxation Parameters*

	Full compression	Normal	SD	PG depleted	SD	*P* value
Proton T1 (sec)	No	1.54	0.06	1.52	0.09	0.658
	Yes	0.99	0.10	1.07	0.09	0.217
(% change)		−35.6	7.9	−29.5	5.8	0.205
Proton T2 (msec)	No	82.4	2.7	90.6	10.6	0.155
	Yes	38.8	2.6	29.6	6.2	0.028
(% change)		−52.9	2.5	−67.1	6.8	0.007
Sodium T1 (msec)	No	24.0	1.6	30.6	2.7	0.003
	Yes	14.8	1.9	24.8	3.4	0.001
(% change)		−38.2	8.2	−19.1	7.0	0.004
Sodium T2 (msec)	No	18.0	3.2	25.7	3.8	0.008
	Yes	11.2	0.8	15.5	2.1	0.009
(% change)		−36.6	8.6	−39.3	4.1	0.548

*Relaxation times are given for proton T1, proton T2, sodium T1, and sodium T2 for cartilage in the normal and mechanically compressed state. A comparison is drawn between these parameters for normal cartilage and cartilage that has been enzymatically treated to induce proteoglycan depletion. Standard deviations of all relaxation times are given in the adjacent columns labeled SD. In each case, five cartilage specimens were used. The relaxation times reported are the corresponding means. In addition to relaxation times, the percent change between the normal and compressed state is given. For each normal vs. PG-depleted comparison, the result of a two-tailed *t*-test is given in the rightmost column, labeled *P*, the value in this column represents the probability that the normal and PG-depleted values could have arisen from sampling a single population.

the verification that enzymatic PG depletion effectively increased cartilage softness. The establishment of cartilage compression and PG depletion permitted an evaluation of PG depletion-induced changes in proton and sodium MR characteristics of cartilage in the normal state and during mechanical compression.

The results of the present study have implications for clinical research in cartilage imaging. Standard clinical proton imaging that employs basic T1 and T2 contrast mechanisms is unlikely to distinguish PG depletion in articular cartilage since we have demonstrated that proton T1 and T2 do not vary significantly with PG depletion. However, we have demonstrated that, when cartilage is in a mechanically compressed state, a significant change in proton T2 does occur with PG depletion. This result indicates that it may be possible to identify regions of articular cartilage that have a low PG content with T2-weighted proton imaging, if the cartilage of interest is in a compressed state. A limitation worth mentioning is that compressed-state proton T2 changes

Table 3
Statistical Significance of the Change in Relaxation Time Constants Associated With Compression

Nuclei	Normal/degraded	Relaxation time constant	*P*value
Proton	Normal	T1	1.60E-05
	Normal	T2	5.00E-09
	Degraded	T1	4.00E-05
	Degraded	T2	3.20E-05
Sodium	Normal	T1	3.50E-05
	Normal	T2	0.0056
	Degraded	T1	0.018
	Degraded	T2	0.002

associated with PG depletion are on the order of magnitude of their standard deviation among samples. Therefore, relaxation time constant, alone, may provide information on relative PG depletion (ie, a measure of cartilage degradation over time) but will require additional information to make an absolute prediction of PG depletion. In vivo, mechanical compression of articular cartilage can be induced physiologically by having subjects perform certain exercises prior to imaging. Experimental evidence supports the notion that the rate of cartilage recovery is slow enough to permit MRI measurements of cartilage thickness dynamics during recovery (20).

The results also support the notion that sodium imaging could have a substantial impact on cartilage evaluation in a clinical setting. We have demonstrated that both sodium T1 and T2 change significantly as a function of PG depletion whether or not the cartilage is in a compressed state. One caveat to this result is that sodium T1 and T2 both increase with PG depletion, and thus each may offset the effect of the other depending on the specifics of an imaging pulse sequence. The sodium relaxation parameters that we report can aid in the development of an optimal sodium pulse sequence for imaging cartilage PG loss.

In addition to clinical implications, the results reported in this study are relevant to understanding the physiological mechanisms of cartilage deformation and NMR relaxation mechanisms in cartilage. For example, the proton relaxation time constants reported here are consistent with those of previous work in which cartilage compression was performed via an osmotic technique prior to MR evaluation at atmospheric pressure (21). The consistency of the present results with those cited indicates that changes in compression-induced proton MR characteristics can be generated by both mechanical or osmotic pressure gradients. This conclusion has implications for in vitro proton MR cartilage studies in that investigators should be careful to match the osmolarity of cartilage tissue culture media with that of synovial fluid. A further implication is that it is possible that baseline measurements of cartilage proton relaxation times in vivo can be influenced by the osmolarity by a subject's synovial fluid.

With the assumption that PG depletion is the primary cause of cartilage softening, these results indicate that it may be possible to infer cartilage softening via an indirect measurement of PG content. As mentioned above, there is no direct way of measuring PG changes using proton MR without resorting to compression. However, using sodium MR, one can indirectly infer changes in PG content, without resorting to compression. Two limitations of using sodium MRI are that it has a lower signal-to-noise ratio and that it requires stronger imaging gradients to resolve thin objects such as cartilage. However, the shorter T1 of sodium can be exploited in signal averaging to improve signal-to-noise ratio. High-quality sodium images of articular cartilage have been acquired in vivo in a research setting (12), which suggests that the technology can be moved toward clinical applications. This inference can then be related to cartilage softening and in turn to a non-compressive assessment of cartilage functionality. Further work in this direction is in progress.

ACKNOWLEDGMENTS

The authors express gratitude to Jennifer Beers for help with proteoglycan assays.

REFERENCES

1. Mccutchin CW. The frictional properties of animal joints. Wear 1972;5:1-17.
2. Armstrong CG, Mow VC. Variations in the intrinsic mechanical properties of human articular cartilage with age, degeneration and water content. J Bone Joint Surg [AM] 1982;64A:88-94.
3. Lesperance LM, Gray MI, Burstein D. Determination of fixed charge density in cartilage using nuclear magnetic resonance. J Orthop Res 1992;10:1-13.
4. Herberhold C, Stammberger T, Faber S, et al. An MR-based technique for quantifying the deformation of articular cartilage during mechanical loading in an intact cadaver joint. Magn Reson Med 1998;39:843-850.
5. Mansour JM, Mow VC. The permeability of articular cartilage under compressive strain at high pressures. J Bone Joint Surg 1976;58A: 505-516.
6. Mow VC, Holmes MH, Lai WM. Fluid transport and mechanical properties of articular cartilage: a review. J Biomech 1984;17:377-394.
7. Basser PJ, Schneiderman R, Bank RA, Wachtel E, Moroudas A. Mechanical properties of the collagen network in human articular cartilage as measured by osmotic stress technique. Arch Biochem Biophys 1988;351:207-219.
8. Mow VC, Kuei Sc, Armstrong CG. Biphasic creep and stress relaxation of articular cartilage in compression: theory and experiments. J Biomech Eng 1980;102:73-84.
9. Lehner KB, Rechl HP, Gmeinwieser JK, Heuck AF, Lukas HP, Kohl HP. structure, function and degeneration of bovine hyaline cartilage: assessment with MR imaging in vitro. Radiology 1989;170:495-499.
10. Rubenstein JD, Kim JK, Henkelman RM. Effects of compression and recovery on bovine articular cartilage: appearance on MR images. Radiology 1996;201;843-850.
11. Kaufman JH, Regatte RR, Bolinger L, et al. A novel approach to observing articular cartilage deformation in vitro via magnetic resonance imaging. J Magn Reson Imaging 1999;9:653-662.
12. Reddy R, Insko EK, Noyszewski EA, et al. Sodium MRI of human articular cartilage in vivo. Magn Reson Med 1998;39:697-701.
13. Bashir A, Gray ML, Burstein D. Sodium T1 and T2 in control and degraded cartilage; implications for determination of tissue proteoglycan content. In: Proceedings of the SMR 3rd Annual Meeting, Nice, 1995. p 1896
14. Jelicks LA, Paul Pk, O'Byrne E, Gupta RK. Hydrogen-1, sodium-23, and carbon-13 MR spectroscopy of cartilage degradation in vitro. J Magn Reson Imaging 1993;3:565-568.
15. Paul Pk, O'Byrne EM, Gupta RK, Jelicks LA. Detection of cartilage degradation with sodium NMR (letter). Br J Rheumatol 1991;30: 318.
16. Farndale RW, Sayers CA, Barret AJ. A direct spectrophotometric microassay for sulfated glycosaminoglycans in cartilage cultures. Connect Tissue Res 1982;9:247-248.
17. Schnall MD, Subramanian VH, Leigh JS, Chance B. A new double-tuned probe for concurrent H1 and P31 NMR. J Magn Reson 1985;65:122-129.
18. Hahn EL. Spin echoes. Phys Rev 1950;80:580.
19. Reddy R, Kaufman JH, Insko E, Kneeland JB, Leigh JS. Sodium spectroscopy of articular cartilage during compression. In: Proceedings of the ISMRM 4th Annual Meeting, New York, 1996. p 1097
20. Eckstein F, Tieschky M, Faber SC, et al. Effect of physical exercise on cartilage volume and thickness in vivo: MR imaging study. Radiology 1998;207:243-248.
21. Lusse S, Knauss R, Werner A, Grunder W, Arnold K. Action of compression and cations on the proton and deuterium relaxation in cartilage. Magn Reson Med 1995;33:483-489.

Magnetic Resonance in Medicine 41:30–34 (1999)

Sodium NMR Evaluation of Articular Cartilage Degradation

Erik K. Insko,* Jonathan H. Kaufman, John S. Leigh, and Ravinder Reddy

One of the first effects of degenerative osteoarthritis is the loss of proteoglycans from the matrix of articular cartilage. Using a model of osteoarthritic change where the cartilage has been enzymatically degraded with trypsin, the sodium NMR characteristics of the cartilage were determined as a function of changes in the proteoglycan content. The results demonstrate that the single quantum sodium signal decreases as the proteoglycan content of the cartilage matrix decreases. In addition, the relaxation characteristics of the sodium change such that the T_1 is longer, the T_{2s} is longer, and the T_{2f} is shorter. Short echo-time, T_1-weighted sodium images are presented which demonstrate that this information may be utilized to detect the loss of proteoglycans from articular cartilage. Magn Reson Med 41:30–34, 1999. © **1999 Wiley-Liss, Inc.**

Key words: sodium; cartilage; osteoarthritis

INTRODUCTION

Articular cartilage functions as the load-bearing surface of all joints. The load-bearing capability is a function of the proteoglycan content of the cartilage matrix. Negatively charged proteoglycans in the matrix of the cartilage increase the concentration of sodium ions present in articular cartilage to levels that may approach 300 m*M* or higher in healthy cartilage (1, 2). The osmotic pressure of the sodium ions provides the cartilage with its load-bearing capability.

In response to IL-1, chondrocytes release metalloproteinases that degrade proteoglycans in the cartilage (3–7). One of the earliest effects of degenerative osteoarthritis is the loss of proteoglycans from articular cartilage (5–7). When the proteoglycan component of the cartilage decreases, there is a simultaneous decrease in the sodium concentration in the cartilage (1, 8). In addition, the loss of the negatively charged proteoglycans from the cartilage may alter the relaxation characteristics of the sodium. Such changes have been demonstrated by sodium NMR (9–11).

The purpose of this paper is to measure the sodium spectroscopic parameters of articular cartilage as a function of changes in the proteoglycan content of the cartilage and to determine which parameters change after the loss of even small amounts of proteoglycans from the matrix of the cartilage. The change in the single quantum sodium signal as a function of changes in the proteoglycan content of cartilage is demonstrated. The change in the T_1 and both components of the sodium T_2, T_{2f} and T_{2s}, as a function of changes in the proteoglycan content of cartilage are also presented. Sodium images are presented which demonstrate that the loss of proteoglycans from the matrix of the cartilage may be detected with single quantum, T_1-weighted, short echo-time methods.

MATERIALS AND METHODS

Cartilage Specimens

Specimens of articular cartilage were cored from fresh bovine patella using a diamond-tipped cylindrical core drill bit (Accuratus Ceramics, Washington, NJ). The resulting disk-shaped specimen was roughly 1 cm in diameter. Nine cartilage specimens were obtained for evaluation. Eight of these specimens were dissected away from the underlying bone and marrow, leaving an approximately 2-mm thick layer of cartilage. These eight specimens ranged in wet weight from 0.23 to 0.33 g and were retained for sodium spectroscopic evaluation: four control specimens and four specimens for degradation. One specimen, with intact underlying bone and marrow, was cut into a rectangle with a scalpel blade. This specimen was 2 mm wide, 4 mm thick, and 1 cm long. This sample was then divided in two pieces of 5 mm length each. These two specimens were retained for sodium imaging evaluation.

Enzymatic Degradation

Proteolytic degradation of the articular cartilage was performed in a trypsin-containing bath. Trypsin degrades proteoglycans by cleaving the core protein into successively smaller units (12). The negatively charged glycosaminoglycans, side chains of the core protein, are liberated from the cartilage in this process. The degradation bath was prepared with a solution of 0.2 mg/ml of trypsin (Sigma Chemical Co., St. Louis, MO) in a phosphate buffered saline solution (150 m*M* sodium chloride) that had been adjusted to pH 7.6. A control solution containing no trypsin was also prepared. Five cartilage specimens were placed in the trypsin bath for 2-h intervals at 30°C and 0.5 Hz agitation. Another five specimens were placed in the control solution for 2-h intervals under equivalent conditions. After each 2-h interval in the bath, the solutions were withdrawn for spectrophotometric evaluation of glycosaminoglycan content (13) and the cartilage was evaluated with sodium NMR: either spectroscopy or imaging. After data acquisition, the cartilage was returned to a fresh solution, either trypsin or control, for another 2-h interval. Five cycles of data acquisition were performed for the specimens that were evaluated spectroscopically. These specimens underwent a total of 10 h of enzymatic degradation during the experiment. Four cycles of data acquisition were performed for the specimens that were evaluated by single quantum sodium imaging. This specimen under-

Stellar-Chance Laboratory, Department of Radiology, University of Pennsylvania, Philadelphia, Pennsylvania.

Grant sponsor: NIH; Grant number: RR-02305.

*Correspondence to: Erik K. Insko, M.D., Ph.D., University of Pennsylvania, Department of Radiology, B-1, Stellar-Chance Laboratory, 422 Curie Blvd., Philadelphia, PA 19104-6100.

Received 27 May 1997; revised 3 June 1998; accepted 5 June 1998.

went a total of 8 h of enzymatic degradation during the experiment.

Spectrophotometric Evaluation

Spectrophotometric evaluation of the glycosaminoglycan content in the degradation solution was performed by adding serial dilutions of the solution to a 5-ml solution of 16 mg/liter dimethylmethylene blue in a buffer of 5 ml/liter ethanol, 2 g/liter sodium formate, and 2 ml/liter formic acid (13). The glycosaminoglycan content of the degradation solutions were determined by observing the change in spectrophotometric absorption at 535 nm and comparing the change with that observed in a set of standard solutions with known concentrations of chondroitin sulfate (Sigma Chemical Co., St. Louis, MO). The total glycosaminoglycan content of each piece of cartilage was determined by enzymatically degrading each piece for 48 h in multiple trypsin solutions, to control for enzymatic autodigestion, after all NMR data were gathered. After this period of time, no additional glycosaminoglycan could be extracted from any of the cartilage specimens.

Sodium Spectroscopy

All NMR experiments were performed in a 2 T whole body magnet (Oxford Magnet Technology, UK) that had been interfaced to a custom-built spectrometer hardware and software package. Each cartilage specimen retained for spectroscopic evaluation was placed at the center of a custom-built 5-turn, 1-cm inside diameter solenoid radiofrequency coil. The coil was tuned to 22.84 MHz, the resonance frequency of sodium-23 at 2 T, using a variable capacitor (Crane, New Rochelle, NY) and fixed capacitors (American Technical Ceramics, Huntington Station, NY).

Sodium spectroscopic evaluation of the articular cartilage was performed to evaluate the single quantum sodium signal, effective T_1, and the two components of the biexponential T_2:T_{2f} and T_{2s} via a triple quantum method. The single quantum signal was obtained from each specimen with a single 90° pulse experiment that averaged 600 acquisitions at a repetition time of 200 ms. The triple quantum sodium signal was obtained from each specimen with a 90°–180°–90°–90° pulse sequence that employed a six-step phase cycling scheme (14). The preparation time, the time between the first two 90° pulses in the sequence, was varied in steps from 0.1 to 30 ms to obtain antiphase biexponential decay data that were subsequently fit to determine T_{2f} and T_{2s}. Each triple quantum data point averaged 600 total acquisitions at a repetition time of 200 ms. The T_1 of the sodium was determined with a 180°–90° inversion recovery sequence. The inversion time, the time between the initial 180° and the 90° observation pulse, was varied in 2-ms increments from an initial value of 2 ms to a maximal value of 100 ms. Each data point was signal averaged 25 times at a repetition rate of 200 ms.

Sodium Imaging

Cartilage specimens were placed into a thin-walled glass tube (Wilmad Glass Co., Buena, NJ) that was positioned at the center of a custom-built 5-turn, 5-mm inside diameter solenoid radiofrequency coil positioned at the center of a custom-built gradient set (15). The coil was tuned as described previously.

Sodium images were obtained with a non-slice selective spin-echo sequence described in detail elsewhere (16). The slice thickness was defined by the thickness of the sample, which was 2 mm. The imaging matrix acquired 128 phase encoding steps and 256 data points in each acquisition. The pulse sequence acquired an asymmetric echo (17) and was reconstructed via a homodyne reconstruction technique (18, 19). The FOV was 3 cm in the phase encoding direction and 1 cm in the frequency encoding direction, which was through the thickness of the cartilage. The echo time was 1 ms. The repetition time was 30 ms. A total of 50 signal averages were acquired in 3 min and 12 s.

Data Analysis

The spectroscopic sodium signal strengths were determined using a principle component analysis algorithm (20, 21). The T_1 of the sodium was determined by fitting the inversion recovery sodium signal as a function of the time between inversion and observation pulses using an adaptation of a nonlinear, least squares fit algorithm (22) to the function

$$S(t) = A(1 - 2e^{-t/T_1}) + B \quad [1]$$

In this function, t is the time between the 180° inversion pulse and the observation pulse for the data observed at each time point, and A and B represent an amplitude and offset level, respectively.

The T_2 values for the sodium, T_{2f} and T_{2s}, were determined by fitting the triple quantum sodium signal as a function of the preparation time in the acquisition sequence. This yields a data set that varies in time as the difference of two decaying exponentials, one of short-time constant, T_{2f}, and one of long-time constant, T_{2s}. The data were fit, using an adaptation of a nonlinear, least squares fit algorithm (22) to the function

$$S(t) = A(e^{-t/T_{2s}} - e^{-t/T_{2f}}) \quad [2]$$

where t was the preparation time in the triple quantum pulse sequence (14) and A is the amplitude.

RESULTS

The cartilage specimens investigated in this experiment were degraded from their original proteoglycan content down to between 50% and 70% of their original content. The single quantum signal and T_{2f} both decreased with proteoglycan degradation, whereas the T_1 and T_{2s} both increased with proteoglycan degradation of the cartilage specimens.

The single quantum sodium signal as a function of the proteoglycan content of the cartilage is shown in Fig. 1. The data demonstrate that the single quantum sodium signal decreased approximately in proportion to the proteoglycan content of the specimens.

The two components of the sodium T_2, T_{2f} and T_{2s}, were determined from fitting the amplitude of the envelope of the triple quantum sodium signal as a function of the preparation time in the triple quantum pulse sequence. Before any enzymatic degradation, the T_{2f} of the cartilage

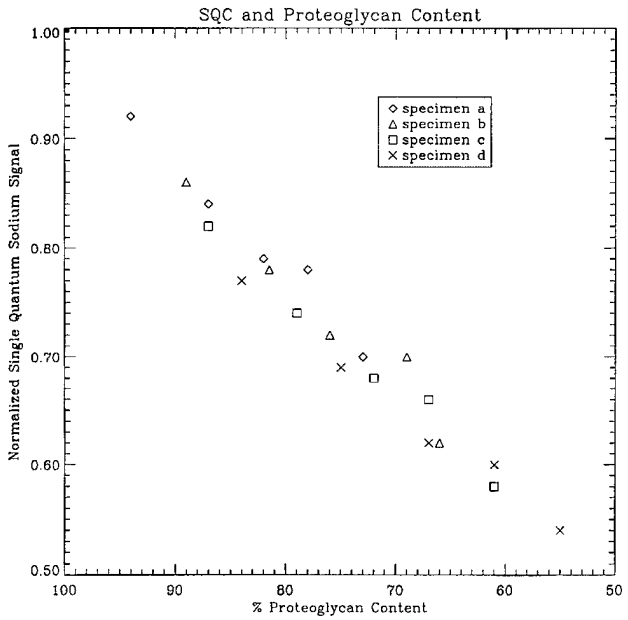

FIG. 1. The normalized SQC (single quantum coherence) sodium signal in the enzymatically degraded cartilage specimens as a function of the measured proteoglycan content remaining in the cartilage after each interval of enzymatic degradation.

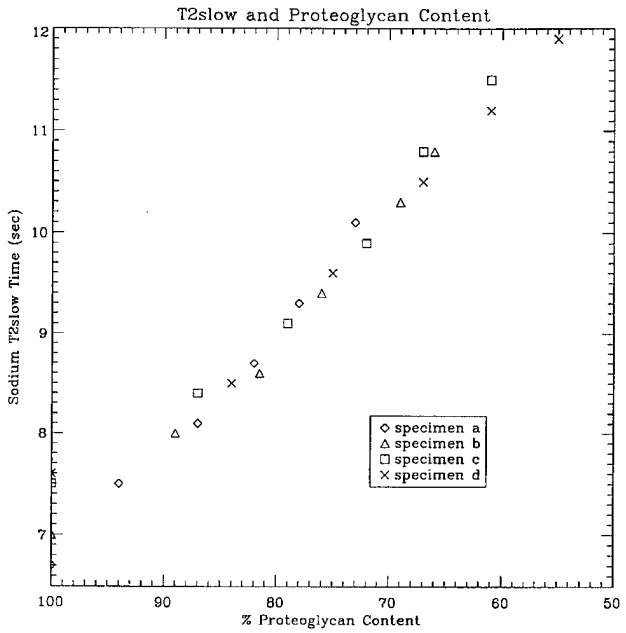

FIG. 3. The T_{2s} of the sodium signal in the enzymatically degraded cartilage specimens as a function of the measured proteoglycan content remaining in the cartilage after each interval of enzymatic degradation.

specimens was 1.9 ± 0.1 ms. The T_{2s} before any degradation was 7.2 ± 0.4 ms. With these values and a delay between the center of the RF excitation pulse and the first data point of 100 ms, the sodium visibility was approximately 94%. The data in Fig. 2 demonstrate that the fast component of the sodium T_2, T_{2f}, reduced slowly with the initial proteoglycan degradation and then somewhat more rapidly as the proteoglycan degradation increased. The data in Fig. 3, however, demonstrate that the slower component of the sodium T_2, T_{2s}, was prolonged as the proteoglycan content of the cartilage decreased.

Before any enzymatic degradation, the T_1 of the cartilage specimens was 17.3 ± 0.6 ms. The T_1 of sodium as a function of the proteoglycan content of articular cartilage is shown in Fig. 4. The data show that the T_1 increased as the proteoglycan content of the cartilage decreased. The change

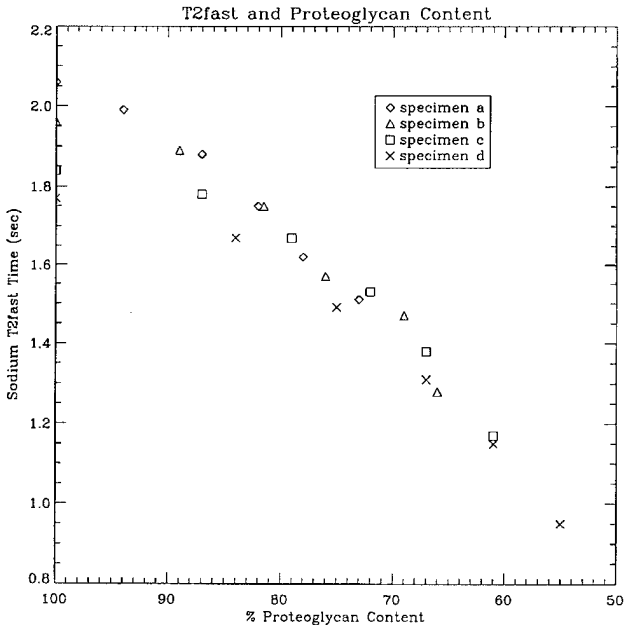

FIG. 2. The T_{2f} of the sodium signal in the enzymatically degraded cartilage specimens as a function of the measured proteoglycan content remaining in the cartilage after each interval of enzymatic degradation.

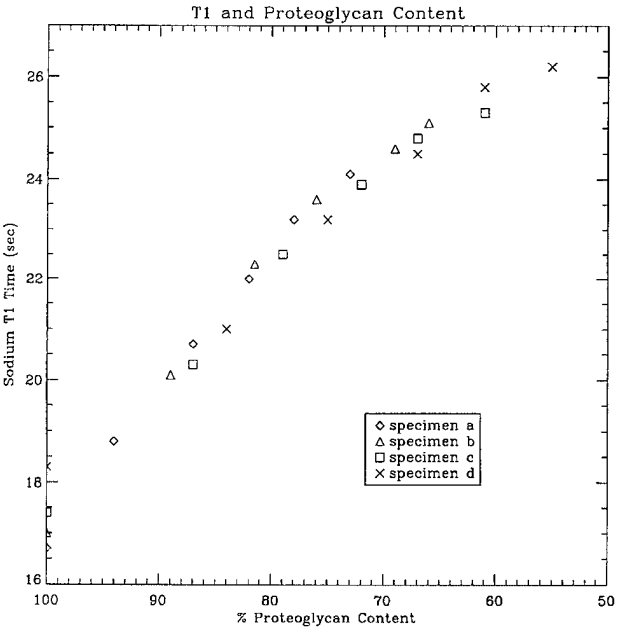

FIG. 4. The T_1 of the sodium signal in the enzymatically degraded cartilage specimens as a function of the measured proteoglycan content remaining in the cartilage after each interval of enzymatic degradation.

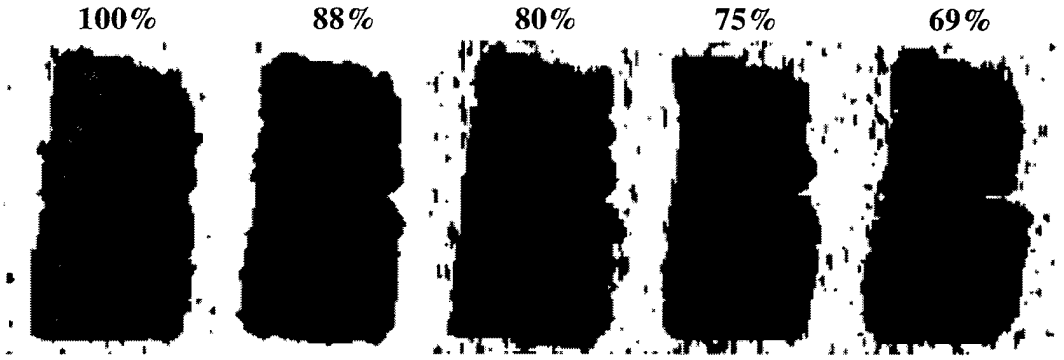

FIG. 5. Single quantum sodium images of a section of articular cartilage that has been divided into two pieces. The top piece in each image has been enzymatically degraded in a trypsin-containing bath at 2-h intervals. The approximate percentage of the proteoglycan content remaining in the top piece is listed above each image. The image repetition time was 30 ms and the echo time was 1 ms.

in the T_1 was clear even after a small degree of cartilage degradation.

Single quantum sodium images of the two cartilage specimens retained for imaging are shown in Fig. 5. The image repetition time and echo time were chosen to maximize the decrease in signal of the enzymatically degraded specimen while still allowing for rapid signal averaging so that high signal-to-noise ratio images can be produced. The images demonstrate that the sodium image intensity decreased significantly in the specimen that was enzymatically degraded. A region-of-image analysis of 200 pixels from the central portion of the cartilage was performed to evaluate changes in image intensity. The results, shown in Fig. 6, give the image intensity as a function of changes in the proteoglycan content of the cartilage.

The loss of signal in the images shown in Fig. 6 is a result of the change in both the sodium concentration and the relaxation characteristics of the sodium. After 8 h of degradation, approximately 31% of the proteoglycan content has been removed and the sodium signal has decreased by approximately 45%. With a 1-ms echo time, a reduction in T_{2f} from 1.9 to 1.4 ms would decrease the image intensity by 21%, and an increase in T_{2s} from 7.2 to 10 ms would increase image intensity by 4%. The exact contribution of these two effects is unknown, however, as the proportion of the sodium in the bound and free pool is unknown. An increase in the T_1 from 17.3 to 24 ms, with a 30-ms repetition time and a 90° excitation pulse, would decrease image intensity by 15%. A change in sodium concentration, which is due to a change in proteoglycan concentration, would decrease the image intensity by approximately 31% at this degree of degradation. A combination of these effects is required to explain the 45% decrease in image intensity observed in this specimen after 8 h of degradation.

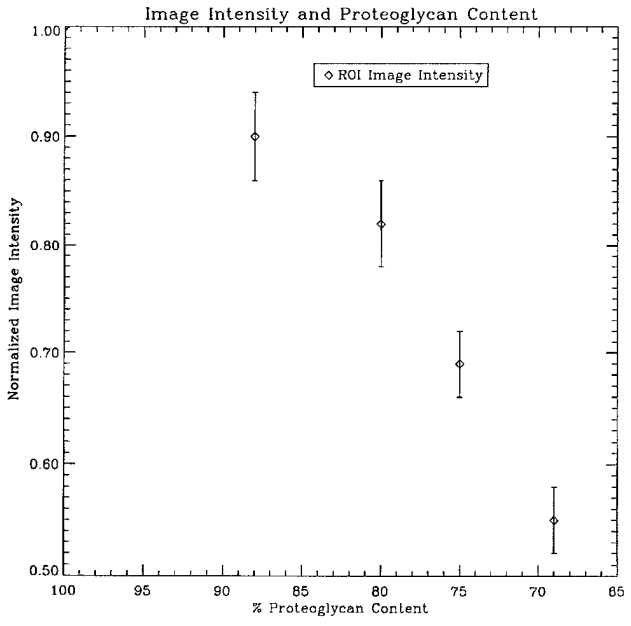

FIG. 6. The normalized signal intensity in a 200-pixel region of interest in the central portion of the image of the enzymatically degraded cartilage specimens as a function of the measured proteoglycan content remaining in the cartilage after each interval of enzymatic degradation. The error bars are the standard deviation of the measurements.

CONCLUSIONS

In this work, we have demonstrated the change in sodium spectroscopic parameters that occur as a function of changes in the proteoglycan content of articular cartilage. The data showed that the single quantum sodium signal decreased approximately in proportion to the proteoglycan content of the cartilage. The single quantum sodium signal is known to change stoichiometrically with the proteoglycan content of the cartilage (1).

The change in the sodium T_1 as a function of changes in the proteoglycan content was demonstrated for the first time. These data revealed that a prolongation of the T_1 occurs with loss of the proteoglycans from the cartilage (10, 11) and that the prolongation of the T_1 occurs even with a small loss of the proteoglycan content of the cartilage. Also, the data revealed a change in the transverse relaxation times, T_{2f} (10) and T_{2s}, with loss of proteoglycans from the cartilage. The changes were demonstrated as a function of changes in the proteoglycan content of the cartilage for the first time. These data revealed that prolongation in T_{2s} also occurs relatively early in the degradation process. The T_{2f}, alternately, became shorter with the loss of proteoglycans from the matrix of the cartilage. This change, however, was only clear with greater levels of proteoglycan loss from the cartilage.

These data demonstrated that certain characteristics of the sodium NMR signal may be exploited to detect the loss of the proteoglycan component of articular cartilage matrix via sodium imaging. Most of the change in the image signal likely arises simply from a decrease in the sodium content of the cartilage secondary to a loss of the proteoglycan content of the cartilage. However, the change in the relaxation characteristics of sodium as a function of the proteoglycan content may also be exploited to formulate an imaging method that could detect only a small loss of proteoglycans from cartilage. The prolongation of the T_1 implies that T_1-weighted images would indicate a greater degree of signal loss in regions of cartilage with a lower proteoglycan content. The lengthening of the T_{2s}, however, will tend to increase the signal from degraded cartilage. Short echo-time images will limit the increase in signal secondary to this effect while still exploiting any reduction in T_{2f} that will act to decrease the signal. Short echo times also retain the adequate signal levels critical in sodium imaging. Single quantum sodium images of cartilage that has undergone serial enzymatic degradation have been presented to demonstrate that this technique may detect the loss of proteoglycans from the cartilage. This indicates that a noninvasive method of detecting the early changes of osteoarthritis may be feasible.

In summary, the loss of proteoglycans from the matrix of articular cartilage may be measured by both single quantum sodium spectroscopy and imaging. The loss of even a small amount of proteoglycans from cartilage also leads to a prolongation of both the T_{2s} and T_1 of the sodium NMR signal. A decrease in the T_{2f} is also detectable with greater amounts of proteoglycan loss from the cartilage. These results indicate that short-echo, T_1-weighted single quantum sodium imaging will detect the early stages of osteoarthritic change in cartilage. Single quantum sodium images of cartilage specimens that have undergone serial proteolytic enzymatic degradation were presented to demonstrate this fact.

REFERENCES

1. Freeman MAR. Adult Articular Cartilage, 2nd ed. England: Pitman Medical Publishing, 1979.
2. Lesperance LM, Gray ML, Burstein D. Determination of fixed charge density in cartilage using nuclear magnetic resonance. J Orthop Res 1992; 10:1–13.
3. Sapolsky AI, Kreiser H, Howell DS, Woessner JF. Metalloproteinases of human articular cartilage that digest cartilage proteoglycan at neutral and acid pH. J Clin Invest 1976; 58:1030–1041.
4. Woessner JF, Selzer MG. Two latent metalloproteinases of human articular cartilage that digest proteoglycan. J Biol Chem 1984; 259:3633–3638.
5. Martel-Pelletier J, Pelletier J-P, Clouteir JM, Howell DS, Ghandur-Mnaymneh L, Woessner JF. Neutral proteases capable of proteoglycan digesting activity in osteoarthritic and normal human articular cartilage. Arthritis Rheum 1984;27:305–312.
6. Ehrlich MG. Degradative enzyme systems in osteoarthritic cartilage. J Orthop Res 1985; 3:170–184.
7. Ralph Schumacher H. Ed., "Primer on the Rheumatic Diseases," 10th ed, Atlanta, Ga: Arthritis Foundation, 1993.
8. Maroudas A, Evans H. A study of ionic equilibria in cartilage. Connect Tiss Res 1972; 1:69–77.
9. Foy BD, Lesperance LM, Gray ML, Burstein D. NMR parameters of interstitial sodium in cartilage, *in* Proc., SMRM, 8th Annual Meeting, Amsterdam, 1989. p. 1108.
10. Bashir A, Gray ML, Burstein D. Sodium T_1 and T_2 in control and degraded cartilage: implications for determination of tissue proteoglycan content, "Proc., SMRM, 14th Annual Meeting, Nice, 1995," p. 1896.
11. Jelicks LA, Paul PK, O'Byrne E, Gupta RK. Hydrogen-1, Sodium-23, and Carbon-13 MR spectroscopy of cartilage degradation in vitro. JMRI 1993;3:565–568.
12. Tyler JA. Cartilage degradation, Cartilage: Molecular Aspects, (Hall B, Newman S, editors), Chapter 7, CRC Press, Boca Raton, 1991.
13. Farndale RW, Sayers CA, Barnett AJ. A direct spectrophotometric microassay for sulfated glycosaminoglycans in cartilage cultures. Conn Tiss Res 1982;9:247–248.
14. Jacard G, Wimperis S, Bodenhausen G. Multiple quantum NMR spectroscopy of S = 3/2 spins in isotropic phase: a new probe for multiexponential relaxation. J Chem Phys 1986; 85(11):6282–6293.
15. Bottomley PA. A versatile magnetic field gradient control system for NMR imaging. J Phys E Sci Instrum 1981; 14:1081–1087.
16. Insko EK, Reddy R, Leigh JS. High resolution, short echo time sodium imaging of articular cartilage. JMRI 1997; 7(6):1056–1059.
17. Provost TJ, Hurst GC. Asymmetric sampling in 2DFT magnetic resonance imaging, *in* "Proc., SMRM, 5th Annual Meeting, Montreal, 1986," p. 265.
18. Macovski A, Noll DC. Homodyne detection for improved SNR and partial *k*-space reconstruction. *in* "Proc. SMRM, 7th Annual Meeting, San Francisco, 1988," p. 815.
19. Oh CH, Hilal SK, Ra JB, and Cho ZH. Faster magnetic resonance imaging by use of 3-quarter matrix data, Proc., SMRM, 6th Annual Meeting, New York, 1987. p. 455.
20. Stoyanova R, Kuesel A, Brown T. Application of principle-component analysis for spectral quantitation. J Magn Reson 1995; A115:256–269.
21. Elliott MA, Walter GA, Swift A, Vandenbourne K, Schotland JC, Leigh JS. Spectral quantification by principle-component analysis using complex single value decomposition, Proc., ISMRM, 6th Annual Meeting, Sidney, 1998, p. 1855.
22. Bevington PR. Data Reduction and Error Analysis for the Physical Sciences, New York: McGraw-Hill; 1969. pp. 237–239.